IEEE Access
Multidisciplinary | Rapid Review | Open Access Journal

Received May 10, 2021, accepted May 15, 2021, date of publication May 25, 2021, date of current version June 4, 2021.

Digital Object Identifier 10.1109/ACCESS.2021.3083703

A Cascaded Classification-Segmentation Reversible System for Computer-Aided Detection and Cells Counting in Microscopic Peripheral Blood Smear Basophils and Eosinophils Images

AMIRA S. ASHOUR[1], MARAM A. WAHBA[1], AND RAMI GHANNAM[2], (Senior Member, IEEE)

[1]Department of Electronics and Electrical Communication Engineering, Faculty of Engineering, Tanta University, Tanta 31527, Egypt
[2]James Watt School of Engineering, University of Glasgow, Glasgow G12 8QQ, U.K.

Corresponding author: Amira S. Ashour (amirasashour@yahoo.com; amira.salah@f-eng.tanta.edu.eg)

ABSTRACT Computer-aided image analysis has a pivotal role in automated counting and classification of white blood cells (WBCs) in peripheral blood images. Due to their different characteristics, our proposed approach is based on investigating the variations between the basophils and eosinophils in terms of their color histogram, size, and shape before performing the segmentation process. Accordingly, we proposed a cascaded system using a classification-based segmentation process, called classification-segmentation reversible system (CSRS). Prior to applying the CSRS system, a Histogram-based Object to Background Disparity (HOBD) metric was deduced to determine the most appropriate color plane for performing the initial WBC detection (first segmentation). Investigating the local histogram features of both classes resulted in a 92.4% initial classification accuracy using the third-degree polynomial support vector machine (SVM) method. Subsequently, in the proposed CSRS approach, transformation-based segmentation algorithms were developed to fit the specific requirements of each of the two predicted classes. The proposed CSRS system is used, where the images from an initial classification process are fed into a second segmentation process for each class separately. The segmentation results demonstrated a similarity index of 94.9% for basophils, and 94.1% for eosinophils. Moreover, an average counting accuracy of 97.4% for both classes was achieved. In addition, a second classification was carried out after applying the CSRS, achieving a 5.2% increase in accuracy compared to the initial classification process.

INDEX TERMS Leukocyte segmentation, white blood cells, peripheral blood image, microscopic image analysis, counting cells, classification, histogram-based segmentation, automatic detection.

I. INTRODUCTION

Blood circulating in the human body is composed of red blood cells (RBCs), white blood cells (WBCs), and platelets. In peripheral blood circulation, WBCs are most prominent. These cells are derived from bone marrow and have a crucial role in protecting the human body and maintaining its immune system [1]. There are main five types of WBCs: eosinophils, monocytes, lymphocytes, basophils, and neutrophils [2]. Both eosinophils, and basophils play a significant role in fighting parasitic infections, mediating allergic reactions, and preventing blood clotting.

The associate editor coordinating the review of this manuscript and approving it for publication was Derek Abbott.

Blood screening is an important testing process that enables pathologists to determine the physical well-being of individuals. It enables them to extract vital information, such as the WBCs type, number, and size, thereby assisting pathologists in diagnosing different diseases that include leukemia, and other blood disorders [3]. A broad series of laboratory tests are considered for evaluating the cells' number in the blood fluid. For example, WBC differential testing is a commonly used medical procedure for a complete blood count (CBC). It is used for determining the absolute count or the relative percentage of each type of the leukocytes to identify potential health issues such as infections, as well as blood disorders based on the deviation of WBC count from its reference range. Conventionally, the process of differential

blood counting is performed by pathologists using manual techniques, such as the blood smear examination. Counting WBCs is performed using a microscope either directly or via a captured image.

Inevitably, the non-uniform distribution of the WBCs across the smear, as well as the human counting errors, leads to inaccurate counting process. Moreover, conventional microscopes used in the manual scanning process are limited by their space-bandwidth product, resulting in a tradeoff between the image's resolution, and the microscope's field-of-view (FoV). For example, for a differential count, a high magnification objective lens is required, which leads to a very small FoV [4]. Despite the presence of more reliable automated counting techniques, such as the flow cytometry-based instruments, these instruments are expensive and are incapable of determining the morphology or shape of the cells. Thus, image processing-based techniques provide an adequate automated solution for both the quantitative and qualitative analysis of the microscopic images [5], [6].

Subsequently, accurate segmentation is considered a crucial step in microscopic image analysis that directly affects feature extraction, classification, and cell counting. Since cell morphology is different in each type of WBCs, numerous segmentation methods were developed in literature [7]–[12]. Each of these methods depends on the WBCs' microscopic imaging characteristics.

Typically, WBCs have a recognizable dark-violet nucleus enclosed by a distinct lilac cytoplasm. However, WBCs have various dimensions, edges, shapes, as well as a presence or absence of granules in the cytoplasm, which further complicates the segmentation and detection process. For example, eosinophils and basophils are granulocytic types, but are different in shape and color. Eosinophils have red-orange granules that are large in size. The basophils are smaller in size compared to the eosinophils, while having irregular shape and dark/large granules [13]. Due to the presence of WBCs with RBCs and platelets in the same microscopic images, recognizing and discriminating WBCs from the surrounding plasma becomes a challenging task using automated cell counters [14]. Moreover, due to illumination inconsistencies, the contrast between the cell contour and its background varies on the basis of different image capturing conditions, which, besides the presence of clumped clusters of overlapping cells, complicates the segmentation task [15].

For peripheral blood cell microscopic image analysis, several studies were devoted to developing a segmentation method for each type of the WBCs, as each type has its unique characteristics, for assisting in a better counting process [14], [16]–[18]. Clustering methods were designed to recognize the cluster that contains the WBCs using different techniques, such as K-means clustering with morphological operators [19], fuzzy C-means clustering [20], and mean-shift clustering to generate island-clustering texture method [21]. On the other hand, the active contour models were employed for segmenting overlapped WBCs [22]–[24]. In addition, since the color of WBC types is different, an adjustment stage is recommended to improve the segmentation process [25]. In some images, the color of the nucleus becomes extremely different from the cytoplasm's color. Accordingly, for enhancing the peripheral blood smear images, several approaches were developed for WBCs segmentation based on color space transformation stage to transfer the color characteristics of the image. A distinctive function was used in the luminance, blue chrominance, and red chrominance (YCbCr) color space followed by the active contour method for segmenting the WBCs' nucleus [25]. Furthermore, the color space decomposition was integrated with the K-means clustering for better segmentation [9]. Considering the nonexistence of the Y component in the cells' images and to overcome the distinctive similarities between the background components and the cytoplasm, the cyan, magenta, yellow, and key plate (CMYK) color space was implemented [9]. Other color spaces were used in the literature, such as the hue, saturation, and intensity (HSI) [26], the International Commission on Illumination color space (CIELAB), where L is the lightness from black to white, A is the value from green to red, and B is the value from blue to yellow, and the luminance, in-phase, quadrature (YIQ) [27]. Without doubt, using an appropriate color space is helpful in any further processes, which includes segmentation, feature extraction/selection, and classification.

Most techniques in the literature only use a segmentation process for performing WBCs cells counting using the connected component labeling [28]. A Gram–Schmidt orthogonalization approach was integrated with the snake algorithm for segmenting the cytoplasm and nucleus of WBCs, which recognized five groups of WBCs in the peripheral blood images [29]. Afterwards, several features were extracted, including the co-occurrence matrix, and the local binary pattern (LBP). Next, feature selection was carried out using the sequential forward selection (SFS) algorithm for improved performance. Finally, a classification process was performed using SVM, and artificial neural network (ANN) [27]. It was concluded that the extracted co-occurrence matrix features required more computational time compared to the textural LBP features. This method achieved an inclusive segmentation of 93% with a classification accuracy range between 90 and 96%. However, due to the needed alignment of the initial vectors in the Gram-Schmidt technique, the main disadvantage of this method was the necessity of applying primary calibration process at the initiation point. Several studies were conducted to improve a complete detection and counting systems for the WBCs [30], [31]. Such studies included a classification stage to determine the different WBC types without performing a preceding segmentation process. Since the segmentation stage improves the accuracy of any further classification process, other studies applied a segmentation process prior to the classification stage, which also speeds-up the classification process.

Inspired by the variety of WBC characteristics [32], and since the segmentation and classification processes are highly related, we aim to establish a new framework by

exploiting the benefits of these variations and incorporating them in a tailored segmentation algorithm for each class. The proposed system adopts an inverse flow compared with traditional computer-aided detection systems. It consists of several phases including two-segmentation (dual-segmentation) processes overlapped with two-classification (dual-classification) processes as a framework to classify a pool of different unclassified types of the WBC's images and to improve the accuracy of the overall microscopic computer-aided diagnosis (CAD) in comparison to previous work in [29]. Due to the importance of the basophils and eosinophils image analysis, the present work applied wavelet thresholding-based segmentation approach to segment both types of WBCs' using different adjustments. This was achieved by inversing the CAD sequence, such that the classification process was executed before the segmentation process, which enabled a tailored segmentation algorithm to be achieved per class.

The organization of the paper is as follows. Section II introduces the proposed system methodology as a general framework of a CAD and counting system of two main types of the peripheral blood smear images. Then, in Section III, the results of the proposed system for basophils and eosinophils detection and counting are included and interpreted. Finally, the conclusions are highlighted in Section IV.

II. METHODOLOGY OF THE PROPOSED SYSTEM FOR BASOPHILS/EOSINOPHILS DETECTION AND COUNTING

The main challenges with designing any computer-aided detection and counting system in microscopic peripheral blood smear images are:

(i) the lack of a unique and efficient segmentation approach for different types of WBCs, and
(ii) the complexity in the classification process due to the presence of the background, which adds noise to the extracted features. Therefore, we aim to overcome these two main problems by developing a new general process framework.

In the first phase, since each type of the WBCs requires specific setting and specific color space for precise segmentation, an initial segmentation process was applied before employing an inverse of the sequence of traditional CAD systems by applying the first classification process before a second segmentation task. Thus, to perform CP_1, an initial segmentation process (SP_1) was proposed for accurate separation of the two classes (types of WBCs). We investigated the different images of both types (basophils and eosinophils) in each color space, namely the red, green, and blue (RGB), the hue, saturation, and value (HSV), the CIELAB and the YCbCr to determine the color plane at which the initial ROI, called ROI_i is distinguishable from the background. Then, the intensity range of the ROI_i in each specific color plane was determined for extracting the histogram-based features. These features were then normalized using min-max feature normalization. Successively, the supervised infinite feature

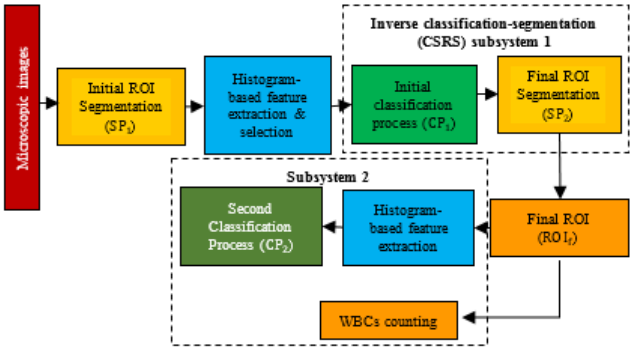

FIGURE 1. General framework of the inverse-based dual-segmentation and dual-classification processes.

selection (Inf-FS) method is used for ranking. Accordingly, the selected features included the bin location of the maximum peak at the sub-histogram, the entropy, and the mean of the normalized green plane histogram at the range. Afterward, CP_1 is performed using these three features as the input of the cubic SVM.

In the second phase, the traditional sequence of the CAD system is followed by using the ROI_i for each type as an input instead of the original image. A wavelet thresholding-based segmentation approach (SP_2, "second segmentation process") was proposed to segment both the basophils and eosinophils images. This segmentation process was based on adjusting the internal parameters of the proposed segmentation method and selecting the suitable color space for each type as follows:

- For the basophils WBCs images, the luminance component of the LAB color space was used as the grayscale image, while the thresholding process was based on obtaining the thresholds from the first-level biorthogonal wavelet transform components and performing the thresholding operation on the reconstructed inverse discrete wavelet transform (IDWT) image.
- For the eosinophils WBCs images, the chrominance component (CR) of the YCbCr color space was used as the grayscale image, where the lightly-colored cytoplasm commonly shares the same luminance levels of the RBCs making them indistinguishable in the luminance color plane. Hence, the approximate component (cA) of the wavelet transform of the Cr color plane was used as the input of the thresholding process to detect the WBC based on the calculated threshold.

The result of this phase is considered the final segmented image determining final ROI_f. Next, ROI_f is used in the counting process and subsequently cascaded into the second (and final) classification process. The phases of the proposed framework are summarized in Fig. 1.

The SP_1 produces ROI_i which feeds CP_1. Based on the classification result, the appropriate segmentation method is used in SP_2 to produce the final ROI_f. Both CP_1 and SP_2 represent the proposed reversible classification-segmentation sub-system 1. Then, the extracted feature set after SP_2 is

used to perform the final classification process, CP_2. Also, ROI_f is used to feed sub-system 2 for counting the WBCs. These two sub-systems form the whole proposed novel CSRS computer-aided detection and counting system framework of basophils and eosinophils cells in microscopic peripheral blood smear images. A detailed explanation of each phase is introduced as follows.

A. PHASE 1: INITIAL WBCS DETECTION AND CLASSIFICATION PROCESSES

The initial WBC prediction process comprises the initial segmentation process SP_1 to find the ROI_f, and the initial classification process CP_1. The determination of the ROI_i is based on an initial estimation of the ROI location and determining the sub-histogram of the ROI_i. Hence, the histogram was used to find the object to background disparity metric. This metric was then used to evaluate the different color spaces for selecting the color space that best represents the rough location of the ROI_i with respect to the image background. This process is performed while preserving the cytoplasmic and nucleus characteristics within the leukocyte (i.e. the ROI_i). This allows the efficient separation and identification of the basophil and eosinophil images in the subsequent classification process CP_1, which is based on the extracted histogram-based features from the segmented ROI_i.

1) HISTOGRAM-BASED OBJECT TO BACKGROUND DISPARITY CALCULATION

The proposed histogram-based object to background disparity (HOBD) metric provides a numerical representation for the visual difference between the ROI_i and the background, which assists in the initial estimation of the ROI location, by determining the most appropriate color plane for this purpose. Consequently, the suitable color channel, which represents the details of the WBCs in the image, is determined. Afterward, the local feature extraction is performed using the selected color plane with the highest HOBD. The HOBD is derived by exploiting the image histogram and locating the sub-histograms of both the ROI_i and the image background.

The object of interest in our study is the WBC, which represents the smallest area (i.e. number of pixels) in the image compared to the background. Thus, in the color planes where the ROI_i is significant, it can be assumed that the sub-histogram with the small area under the curve represents the ROI_i. The ROI_i sub-histogram can be located accordingly. Calculating the HOBD metric involved a two-fold criteria, namely:

(i) measuring the discrepancy apart of the image background, which was the general objective; and
(ii) considering that the ROI_i of both classes are presented by a wide multi-intensity sub-histogram, which allows the extraction of significant local features from the ROI_i of both classes. This allows efficient discrimination between the types of the WBCs at the classification process.

Figure 2 shows the smoothed histogram of an eosinophil image in both the RGB and the YCbCr color spaces, illustrating the parameters used for the HOBD calculation. To calculate the HOBD for a certain color plane, the histogram of the color plane was initially smoothed using a moving average low pass filter to remove the outliers and spikes. Therefore, the histogram contour was obtained, as shown in Fig. 2. The number of the passed parameters to the low pass filter was equal to the reciprocal of the span, which is the number of input elements (data points) that are included in the calculation of each output element in the smoothed histogram to perform the averaging process. Based on trial and error, this parameter was set to 5 points, which achieved a good tradeoff between the computational time and the integrity of the small required variations in the initial ROI sub-histogram. To fulfill the first criterion, two metrics were evaluated, namely the proposed absolute distance between the highest peak at the sub-histogram, and the highest peak at the background sub-histogram P_D, and the traditional image contrast. The proposed absolute peak distance P_D is calculated using the following formula:

$$P_D = |b(H_1) - b(H_2)| \tag{1}$$

where $b(.)$ is the histogram bin location of the peak. Moreover, H_1 and H_2 represent the highest peaks of the ROI_i sub-histogram and the background sub-histogram, respectively. During the calculations of H_1 and H_2 values, two cases were observed regarding the distribution of peaks across the histogram, as shown in Fig. 2.

In the first case, the histogram peaks were distributed over both the right and left halves of the histogram, as shown in Fig. 2(a)-(d), indicating that the image spanned a wide intensity range. In the second case, the histogram peaks were located at one end of the histogram as shown in Fig. 2(e)-(f) indicating less variation in the intensity levels between the ROI_i and the background. These two cases were then used to identify the WBCs type in the image.

To distinguish between both cases, the peak distribution over the intensity range was estimated by means of λ, which represents the product of the number of peaks over the two halves of the intensity range, i.e. from 0-127 and from 128-255. Accordingly, in the first case, $\lambda \neq 0$ and the maximum peaks H_1 and H_2 can be determined as the maximum peak values of the two halves of the histogram range from 0 to 127, and from 128 to 255. However, in the second case, where $\lambda = 0$, H_1 and H_2 were estimated based on the existing number of peaks, as these peaks may be positioned in one half of the histogram range, as shown in Fig. 2(f). Hence, H_1 and H_2 were calculated as follows:

$$H_1 = \begin{cases} \max\{p(x) : 0 \leq b(p) \leq 127\} & \lambda \neq 0 \\ \max\left\{p(x) : x = 1, .., \frac{N}{2}\right\} & \lambda = 0 \end{cases} \tag{2}$$

$$H_2 = \begin{cases} \max\{p(x) : 128 \leq b(p) \leq 255\} & \lambda \neq 0 \\ \max\left\{p(x) : x = \frac{N}{2} + 1, .., N\right\} & \lambda = 0 \end{cases} \tag{3}$$

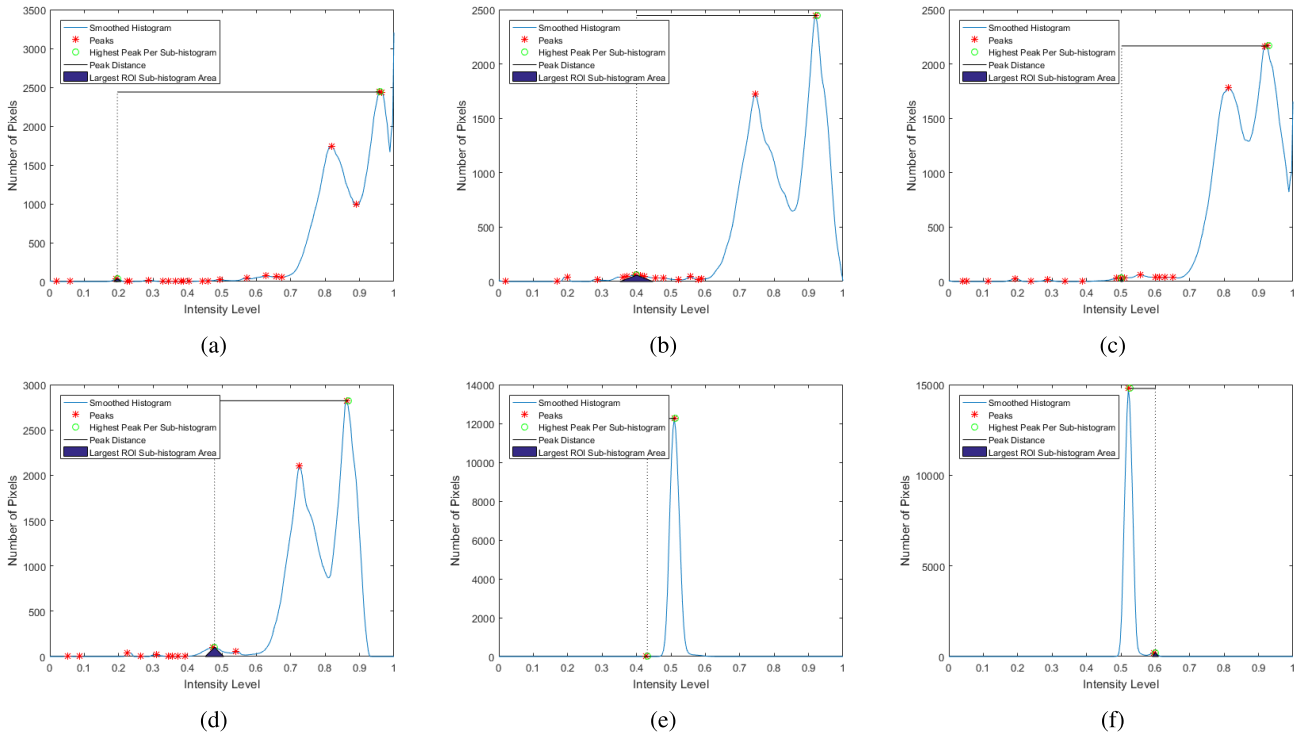

FIGURE 2. Smoothed histogram of eosinophil cell image in different color planes: (a) Red; (b) Green; (c) Blue of RGB color space; (d) Luminance; (e) Blue Chroma; (f) Red Chroma of YCbCr color space.

where $p(x)$ is the peak amplitude, $b(p)$ is the bin location of the peak, $x = [1, .., N]$ is the index of the peak, and N is the total number of the existing peaks. Moreover, the image contrast was evaluated for the intensity image Y of R rows, C columns, and brightness level B as follows:

$$\text{Contrast} = \sqrt{\frac{1}{RC}\sum_{i=1}^{B}\sum_{j=1}^{C}[Y(i,j) - B]^2} \tag{4}$$

$$B = \frac{1}{RC}\sum_{i=1}^{B}\sum_{j=1}^{C}[Y(i,j)] \tag{5}$$

where the pixel-row index is $i = 1, 2, .., R$, and the pixel-column index is $j = 1, 2, .., C$.

The second criterion aims to assign higher weight value to the color space which provides the best representation of the intensity variations of the ROI_i, allowing the extraction of significant features from both WBCs' classes for efficient classification. Therefore, the area under the sub-histogram A_R represents the sub-histogram distribution, which is the blue shaded area in Fig. 2. This area under the ROI_i sub-histogram was calculated using the following proposed formula:

$$A_R = \min[\max(P_F \circ W_F), \max(P_s \circ W_S)] \tag{6}$$

where W_F and W_S are the peak width matrices, P_F and P_S are the matrices of the intensity levels of the peaks at the first and second halves, respectively, and $\circ$ is the Hadamard product operator, which ensures the element-wise multiplication between each peak in the intensity level matrix and its corresponding width. So, the peak amplitude matrices P_F and P_S were estimated as follows:

$$P_F = \begin{cases} p(x) : 0 \le b(p) \le 127 & \lambda \ne 0 \\ p(x) : x = 1, .., \frac{N}{2} & \lambda = 0 \end{cases} \tag{7}$$

$$P_S = \begin{cases} p(x) : 128 \le b(p) \le 255 & \lambda \ne 0 \\ p(x) : x = \frac{N}{2} + 1, .., N & \lambda = 0 \end{cases} \tag{8}$$

Therefore, A_R was calculated using the element-wise Hadamard product between each peak amplitude and its corresponding width. A data point was considered as a local peak if it had a larger value than its two neighboring samples. This criterion ensured the detection of peaks within the initial ROI sub-histogram that had small variations. The peak's width was defined as the distance between the points to the right and left of the peak. The smoothed histogram intercepted a reference line placed beneath the peak at a vertical distance equal to half the peak prominence. Therefore, the peak amplitude and width represent the height, and width of a triangle, respectively, whose area was defined by the area under the peak. The maximum area under the peak for the sub-histogram represents the portion of the with the highest intensity spectrum in terms of both the intensity levels and range. Nevertheless, as the ROI_i sub-histogram could be located at either halves of the intensity range, the maximum area under the peak was estimated at both sides

of the histogram, representing A_R, and the area under the background sub-histogram. In consequence, the minimum of these two values is determined as A_R. Finally, the HOBD can be calculated as the product of the absolute peak distance P_D, the area under the ROI_i sub-histogram A_R, and the image contrast, as follows:

$$\text{HOBD} = P_D \cdot A_R \cdot \text{Contrast}^2 \tag{9}$$

Figure 2 establishes that the green channel encompassed the largest A_R followed by the luminance channel of the YCbCr, while the other channels encompassed an infinitesimal A_R.

Moreover, the highest absolute peak distances P_D were observed, in descending order, at the red, green, blue RGB channels, followed by the luminance channel. Based on the calculated HOBD values including these two parameters, and the image contrast, the green channel exhibits the highest HOBD, which indicates its capability to represent the intrinsic characteristics of the ROI_i in both classes, while distinguishing the ROI_i apart of the image background. Consequently, the green channel was designated for the feature extraction process to obtain the initial classification CP_1 of the WBC images.

2) HISTOGRAM-BASED FEATURE EXTRACTION

Based on evaluating the ROI_i at the green channel for both classes, it was observed that the ROI_i is commonly located at intensity values ranging from $\alpha_1 = 0.2$ and $\alpha_2 = 0.6$. As a result, the histogram-based features were used to extract information related to the gray level distribution within this range (between α_2 and α_2) of the ROI_i sub-histogram. Hence, seven first-order statistics were used: mean, variance, skewness, kurtosis, energy and entropy [33], [34], in addition to the proposed bin location of the maximum peak at the sub-histogram, which is derived from the HOBD calculation. These statistics were based on the probability density of occurrence of the intensity levels, such that the probability density of occurrence of a certain intensity level is estimated as the ratio between the number of pixels having this intensity level to the total number of pixels, both within the ROI_i. Based on the definition of probability density function, the mean was calculated as follows:

$$M = \sum_{\delta=0}^{N_L-1} \rho(\delta) \cdot \delta \tag{10}$$

where $\rho(\delta)$ is the probability density of occurrence of the intensity levels (δ) such that $0 \leq \delta \leq N_L - 1$, where N_L is the number of the possible intensity levels. The central moments μ_k at $k = 2, 3, 4$ represent the variance, skewness, and kurtosis, respectively, which were derived as follows:

$$\mu_k = \sum_{\delta=0}^{N_L-1} (\delta - M)^k \cdot \delta \tag{11}$$

Hereby, the variance measures the deviation of the intensity levels from the mean, while the skewness measures the degree of the sub-histogram asymmetry around its mean, and the kurtosis reflects the sharpness of the intensity level distribution relative to a normal distribution. Nevertheless, the energy reflects the uniformity of the intensity level distribution, which can be considered as follows:

$$\text{Energy} = \sum_{\delta} (\rho(\delta))^2 \tag{12}$$

In contrast, the entropy represents the randomness of the distribution, since smooth distributions result in low entropy values, which can be calculated using the following expression:

$$\text{Entropy} = -\sum_{\delta} \rho(\delta) \cdot \log(\rho(\delta)) \tag{13}$$

Moreover, the proposed bin location of the maximum peak at the ROI_i sub-histogram $\alpha_{\max}$ was estimated using the following proposed formula:

$$\alpha_{\max} = b(\max(p(x))) \tag{14}$$

Despite the extracted feature vector is low-dimensional having only seven features, the optimal feature combination selection requires the exclusion of irrelevant and noisy features for improving the classification CP_1 performance. Consequently, feature selection was applied to select the most significant features for further use in CP_1.

3) SUPERVISED INFINITE FEATURE SELECTION

Although the extracted feature vector comprises only seven features estimated from the ROI_i which may contain noisy irrelevant features. For that reason, a feature selection process was applied, which targeted the selection of informative features while excluding the irrelevant and redundant ones.

Typically, feature selection algorithms can be categorized according to their feature subset evaluation strategy into filter, wrapper, and embedded methods [35]. Filter methods evaluate features' significance according to the intrinsic statistics of the given data, which ensures wider applicability and better generalization without exploiting the potentials of a specific classifier. Hence, the infinite feature selection (Inf-FS) filtering approach was used due to its flexibility and independence from the data scenarios, especially for the cases of noise, interclass overlap and unbalanced classes [36]. Feature ranking using Inf-FS was performed via two steps. Firstly, a weighted undirected fully connected graph was developed, such that its nodes represent the features, and its edges represent the relations between them. The adjacency matrix $A_J(f_m, f_n)$ of the graph was derived for each feature pair (f_m, f_n) to represent the significance of both features and their eligibility to be selected as good candidates. For the calculation of $A_J(f_m, f_n)$, three parameters were estimated for each feature, namely the fisher criterion h_m, the normalized mutual information (u_m), and the standard deviation σ_m. These three parameters were weighted linearly, resulting in the score s_m, which determines the uniqueness of the feature, as in being not redundant, and its relevancy with respect to

other classes using h_m, and both u_m and σ_m, respectively. Subsequently, the adjacency matrix for a feature pair is given by [36]:

$$A_J(f_m, f_n) = s_m \cdot s_n \tag{15}$$

Secondly, a path of length l was formed between the nodes of features f_m and f_n passing through generic nodes whose number is less that the total number of given features. Moreover, several paths of length l can link the features f_m and f_n. At a given path l, the single feature evaluation score can be obtained by [36]:

$$c_l(m) = \sum_{n \in V_N} R_l(m, n) = \sum_{n \in V_N} A_j^l(m, n) \tag{16}$$

where R_l represents the overall contribution of all the possible l length paths, and V_N is the node set representing the given features. The significance of a candidate feature is reflected by the value of c_l in a directly proportional manner. To reduce the computational complexity, the path length was expanded to infinity. Thus, the regularization parameter was incorporated to avoid the divergence caused by summing infinite A_j^l terms as $c(m) = \sum_{l=1}^{\infty} c_l(m)$. Subsequently, the final ranking scores $\tilde{c}(m)$ for each feature can be obtained by [36]:

$$c(\tilde{m}) = [\tilde{C}e]_m \tag{17}$$

$$\tilde{C} = (\mathrm{I} - rA_J)^{-1} - \mathrm{I} \tag{18}$$

where the matrix $\tilde{C}$ encodes the partial scores of the extracted features, e is a one-dimensional vector of ones, while I denotes the identity matrix, and r represents the regularization parameter.

4) FIRST CLASSIFICATION USING SUPPORT VECTOR MACHINE

The SVM is a supervised learning mode that analyzes the input data for either classification or regression tasks using its associated learning algorithms. In the training phase, the objective of the SVM is to obtain the optimal hyper-plane ''decision boundary'' providing the best separation between the given classes. It determines the classification decision at the testing phase based on the position of the applied data sample with respect to the decision boundary. In most cases, the data points are not linearly separable. The SVM method can isolate nonlinearly separable data points by transforming their feature vectors from low-dimensional into high-dimensional vectors. The SVM was trained using the high-dimensional vectors. Nevertheless, the main drawback of this method, especially when handling a large dataset, is its high complexity and time consumption. This leads to the use of the kernel function method [37]. In this work, the SVM method was considered as the main classification system at both CP_1 and CP_2 representing the initial and second classification processes, respectively.

Several polynomial and Gaussian kernels were also investigated for finding the optimal hyper-plane for the given non-linear data. For example, a 5-fold cross-validation resampling method was applied to evaluate the system's performance. This CP_1 was considered the first stage in the proposed reverse classification-segmentation sub-system. Based on this first classification results, each type of the WBCs has its main characteristics, which requires specific adjustment in the final/general segmentation SP_2, which is considered the last stage in the proposed reverse classification-segmentation sub-system to find ROI_f.

B. PHASE 2: FINAL WBC DETECTION BASED ON WAVELET- BASED THRESHOLDING SEGMENTATION

The different characteristics of the basophil and eosinophil images have motivated the development of a unique segmentation algorithm for each class to best fit its inherent color distribution. For basophils, it is difficult to distinguish the bi-lobed nucleus from the cytoplasm, since the purplish-black cytoplasmic granules take up the entire cell. In contrast, for eosinophils, the bi-lobed nucleus can be distinguished from the dark pink stained cytoplasmic granules. However, comparing the WBCs in both classes to the ambient RBCs makes the eosinophil segmentation task more challenging due to the closeness of the RBCs color to the color distribution within the eosinophil. Hence, these inter-class variations should be addressed using the proposed multi-class wavelet-based thresholding segmentation. For instance, the relatively close chrominance values between the dark-violet granules of the basophils and the purplish surrounding RBCs imposed the adoption of the luminance color plane for the RGB to grayscale image conversion. In contrast, the chrominance color plane presented an adequate solution for the segmentation of the red-orange eosinophil from the surrounding purplish RBCs. As follows the final ROI detection for both classes, basophil and eosinophil, was presented based on the general framework of the wavelet-based segmentation in the SP_2 namely $SP_{2-\mathrm{Baso}}$ and $SP_{2-\mathrm{eosino}}$ respectively.

In the $SP_{2-\mathrm{Baso}}$ (Algorithm 1), the predicted RGB basophil images $Y_B = [y_B(1), .., y_B(t_B)]$, where t_B is the number of the predicted basophil images, are initially converted to grayscale. Hence, for each input image $y_B(q)$ where $1 \leq q \leq t_B$, the RGB image was transformed into the CIELAB color space. Next, the dimensionality reduction technique of principal component analysis (PCA) was applied on the luminance component L to emphasize the significant variations among the image pixels using the scores of the principal component that represents the maximum variance direction through the given pixels [38], [39]. Furthermore, PCA adds robustness against the non-uniform illumination that is common in microscopy [40], [41]. The scaled PCA score values were assigned as the intensity levels of the grayscale image's pixels. Afterwards, a single-level two-dimensional (2-D) wavelet decomposition-based thresholding was applied on the scaled grayscale image G_S using the biorthogonal wavelet family to obtain the four wavelet coefficients, namely the approximation cA and the horizontal cH, vertical cV, and diagonal cD details. Then, the global threshold [42] was

calculated for each of the four wavelet components to obtain T_A, T_H, T_V and T_D. These four thresholds were considered in computing the final threshold T_f, which represents their sum divided by a divisor D_v, which is equal to two. The selection of the divisor $D_v = 2$ was experimentally validated in section 3. Subsequently, the inverse single-level 2-D wavelet transform was applied to obtain the recovered image V, which was then quantized using the obtained T_f providing the binary image that indicates the ROI_f. Afterwards, morphological post-processing operations were carried out to obtain the final segmented image $s_B(q)$ representing the $\text{ROI}_{\text{f}-\text{Baso}}$. These operations include:

(i) suppression of the light structures attached to the image borders using 8-bit connectivity neighborhood "8-connected pixels", which satisfies the tradeoff between operation efficiency and the integrity of any WBCs located near the border,
(ii) finding the connected components to determine closed areas and excluding any artifacts having a predetermined area of under 500, which is deduced from experimental trial and error;
(iii) applying morphological closing using a disk-shaped structuring element to connect the disconnected regions in the segmented region; and
(iv) applying a flood-fill operation to fill any remaining holes in the segmented WBCs. The number of connected regions $n_B(q)$ in the final obtained mask $s_B(q)$ was also counted to provide the count of the segmented basophil cells in the original image.

The proposed approach of wavelet-based thresholding segmentation for basophil images is outlined below in Algorithm 1.

In the $\text{SP}_{2-\text{eosino}}$ (Algorithm 2), the predicted RGB eosinophil images are denoted as $Y_E = [y_E(1), .., y_E(t_E)]$, where t_E is the number of the predicted eosinophil images. In this algorithm, the red chrominance plane Cr of the YCbCr color space is considered as the grayscale representation of the input RGB images. Subsequently, the single-level 2-D wavelet decomposition-based thresholding was applied to the Cr plane producing the four wavelet coefficients. Using the same criteria as in Algorithm 1, the threshold was applied to obtain the four thresholds T_A, T_H, T_V and T_D by which the final threshold T_f was computed, as their sum divided by a divisor $D_v = 2$. In contrast to Algorithm 1, the approximation wavelet component cA was quantized using the obtained final threshold T_f rather than the recovered image V as performed in Algorithm 2. In the morphological post-processing, the light structures that are attached to the image borders were suppressed based on 8-bit connectivity neighborhood, and the connected components were determined to exclude any closed-area artifacts of areas less than 500. Thus, the final segmented image $s_E(q)$ representing $\text{ROI}_{\text{f}-\text{eosino}}$, and its WBC count $n_E(q)$ were obtained. The proposed approach of wavelet-based thresholding segmentation for eosinophil images is reported in Algorithm 2 as follows.

Algorithm 1 Proposed Wavelet-Based Segmentation for Basophil Images ($\text{SP}_{2-\text{Baso}}$)

Input: $Y_B = [y_B(1), .., y_B(t_B)]$
Output: $S_B = [s_B(1), .., s_B(t_B)]$, $N_B = [n_B(1), .., n_B(t_B)]$
`// Start Processing`
for $q \leftarrow 1$ to t_B **do**
Transform $y_B(q)$ RGB image into LAB color space to obtain the L colour plane.
Apply the PCA to obtain the score of the pixels in the L colour plane.
Obtain the grayscale pixels as the scaled PCA score values.
Obtain the scaled grayscale image G_S by scaling the grayscale pixels to be in the range of 0 to 1.
`/* Two-dimensional wavelet decomposition-based thresholding */`
Apply single-level discrete 2-D wavelet decomposition on G_S using biorthogonal wavelet to obtain the four wavelet coefficients.
Calculate the threshold for each of the four wavelet coefficients.
Calculate the final threshold $T_f = (T_A + T_H + T_V + T_D)/D_v$, $D_v = 2$.
Apply the single-level inverse discrete 2-D wavelet transform to obtain V.
Quantize V using the final threshold T_f to obtain binary image.
`/* Post-processing */`
Suppress the light structures connected to the binary image borders using 8-bit connectivity neighborhood.
Find the connected regions' area and exclude regions of area < 500.
Apply morphological closing using disk-shaped structuring element whose radius = 2.
Apply flood-fill operation to fill any present holes in the closed image to obtain the segmentation mask $S_B(q)$.
Count the number of connected regions to obtain the number of segmented WBCs ($n_B(q)$).
end for
Find S_B and N_B

Once the SP_2 is closed for both WBCs types to obtain the ROI_f of both classes, namely $\text{ROI}_{\text{f}-\text{Baso}}$ and $\text{ROI}_{\text{f}-\text{eosino}}$ as well as obtaining the counting of the WBCs for each type based on the inputted microscopic image, the final phase of the classification CP_2 was performed to improve the initial classification's results of CP_1 using third-order polynomial SVM. The CP_2 classification process was performed using the same selected histogram-based features at CP_1 to show the impact of the enhanced segmentation output at SP_2 on the classification process compared to SP_1 using the same selected features.

Algorithm 2 Proposed Wavelet-Based Segmentation for Eosinophil Image ($SP_{2-eosino}$)

Input: $Y_E = [y_E(1), .., y_E(t_E)]$
Output: $S_E = [s_E(1), .., s_E(t_E)]$,$N_E = [n_E(1), .., n_E(t_E)]$
`// Start Preprocessing`
for $q \leftarrow 1$ to t_E **do**
Transform the $y_E(q)$ RGB image into YCbCr color space to obtain the Cr color plane.
`/* Two-dimensional wavelet decomposition-based thresholding */`
Apply single-level discrete 2-D wavelet decomposition on Cr using biorthogonal wavelet to obtain the four wavelet coefficients.
Calculate the threshold for each of the four wavelet coefficients.
Calculate the final threshold T_f.
Quantize the cA using the final threshold T_f to obtain binary image.
`/* Post-processing */`
Suppress the light structures connected to the binary image borders using 8-bit connectivity neighborhood.
Find the connected regions' area and exclude regions of area < 500 to obtain the segmentation mask $s_E(q)$.
Count the number of connected regions to obtain the number of segmented WBCs ($n_E(q)$).
end for
Find S_E and N_E.

C. PROPOSED CLASSIFICATION-SEGMENTATION REVERSIBLE COMPUTER-AIDED DETECTION AND COUNTING SYSTEM FRAMEWORK FOR DETECTING AND COUNTING BASOPHILS AND EOSINOPHILS

The proposed CSRS exploits the intrinsic characteristics of the WBC images for tuning the segmentation process. In this work, the basophils and the eosinophils are considered as a case study at which the main objective is to propose the tailored segmentation algorithms, for each microscopic specimen type, which are proposed based on the initial classification CP_1 prediction. Hereby, the proposed system comprises two main stages during the implementation, the training phase and the testing phase as demonstrated by Fig. 3. The objectives of the training phase are to:

(i) determine the location by evaluating the different color spaces and selecting the most significant one by calculating the proposed histogram-based object to background disparity metric;
(ii) segment the original microscopic image to find ROI_i by using the histogram bins that represent the upper and lower boundaries of its sub-histogram;
(iii) extract and select the most distinctive histogram-based features from ROI_i to be used in the initial classification process CP_1; and

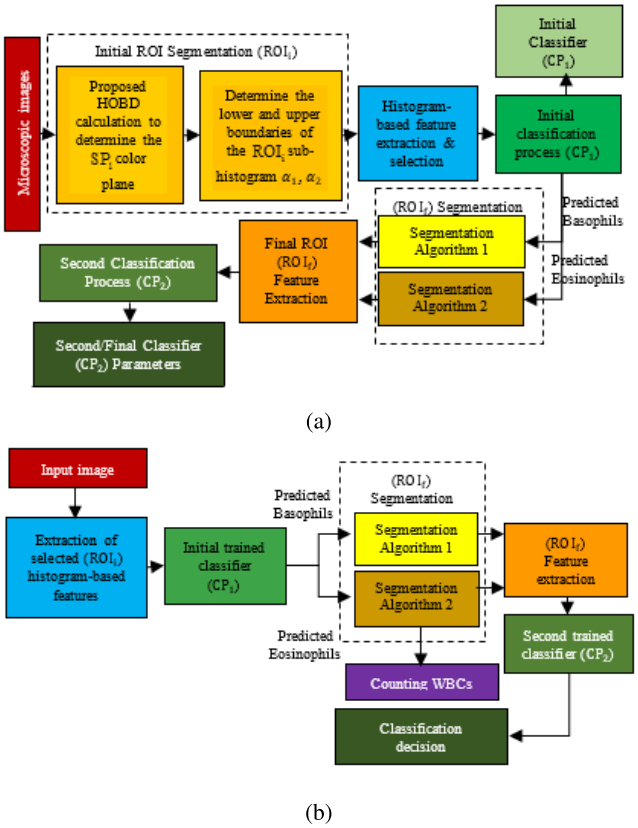

FIGURE 3. Detailed block diagram of the proposed classification-segmentation reversible system: (a) training phase; (b) testing phase.

(iv) train the CP_1 and CP_2 classification systems to set their hyper parameters for the best performance.

The training process of the CP_2 is based on inputting the selected histogram-based features from the segmented ROI_f. The proposed classification-segmentation reversible system for detecting and counting the WBCs is illustrated in Fig.3.

Accordingly, the intention of the first classification process was to accurately determine the WBC class based on the extracted features from the ROI_i, which involves assigning each class to its corresponding segmentation algorithm. Moreover, the second classifier by applying CP_2 would efficiently provide the final classification decision based on the extracted features from the segmented ROI_f. In the testing phase, the initial trained classifier uses the extracted selected features from ROI_i to decide the subsequent segmentation algorithm based on the classification decision. Afterward, the number of WBCs in the segmented image was counted to aid the diagnostic procedure of the hematologist. Therefore, the second trained classifier exploits the extracted features from ROI_f to efficiently determine the class of the input WBCs.

III. EXPERIMENTAL RESULTS AND DISCUSSION

The proposed system was evaluated using the basophil and eosinophil images from the leukocyte images for segmentation and classification (LISC) dataset [43]. This dataset

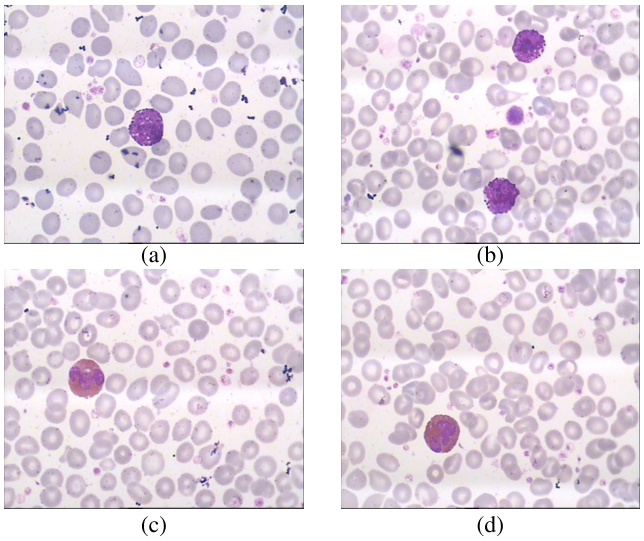

FIGURE 4. Sample images from the dataset: (a) Baso (Image #6); (b) Baso (Image #7); (c) Eosino (Image #12); (d) Eosino (Image #13).

includes digital images of the peripheral blood samples from microscopic slides. It includes manually segmented ground-truth images for proper system evaluation. The used dataset consists of 53 basophil (Baso) and 39 eosinophil (Eosino) images having a resolution of 720 × 576 pixels. However, images were initially resized by half to decrease the run time, while sustaining adequate resolution. Sample images from the applied dataset are displayed in Fig. 4.

A. PHASE 1: INITIAL WBC DETECTION AND CLASSIFICATION PROCESSES

The initial classification process is geared towards distinguishing the images of the two given classes apart to feed the classified image into its specific segmentation criteria (i.e. Algorithm 1 or Algorithm 2) based on the given classification result. The main challenge was to find an approach to extract local features from the WBCs only, excluding the background, while using the whole image. Thus, several color spaces, such as the RGB, HSV, CIELAB and YCbCr were investigated to determine the color plane at which the highest discrepancy occurs between the ROI and the image background. Subsequently, the color plane whose histogram had the highest HOBD was used to extract the histogram-based features, which was performed after estimating the lower and upper boundaries (α_1, α_2) of the histogram bin locations where the ROI_i resides in between.

Figure 5 illustrates a sample eosinophil image displayed in the RGB, HSV, CIELAB and YCbCr color spaces. The visual observation of the images in Fig. 5 showed that the green RGB (G-RGB) color plane presented the highest HOBD, followed by the L- CIELAB and the B- CIELAB color planes, respectively. This observation matches the observation from Fig. 2 for the same image. On the other hand, the H-HSV color plane demonstrated the least visual discrepancy between ROI_i and the image background, as the ROI_i presents similar hue level to the remaining blood cells.

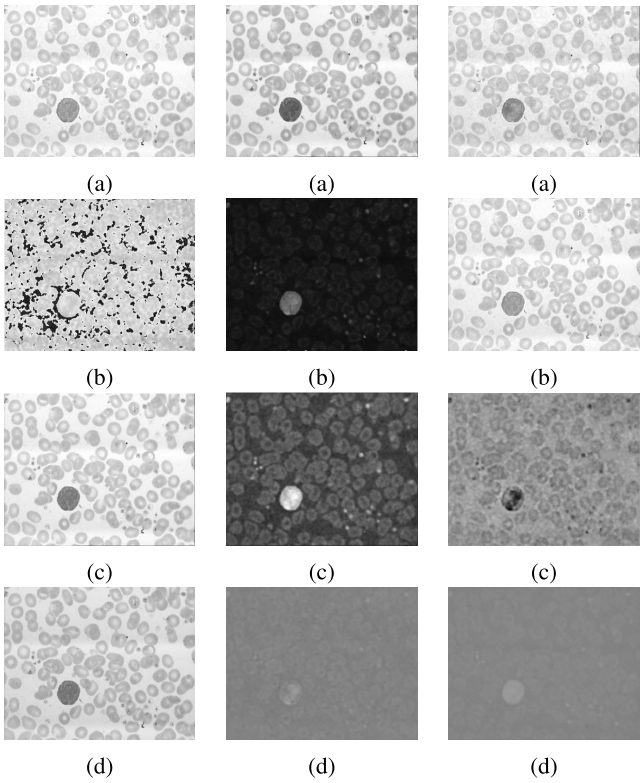

FIGURE 5. Color planes of sample image (Eosino image #13) in different color spaces: (a) RGB color space; (b) HSV color space; (c) CIELAB color space; (d) YCbCr color space where the left column represent the first plane of each color space, the middle column represent the second plane, and the right column represent the third plane.

These findings were numerically established by the calculation of the HOBD metric, as shown in Table 1 in correspondence to the sample images displayed in Fig. 4. Table 1 established that the G-RGB color plane had the highest HOBD followed by the Y-YCbCr color plane, which is the same conclusion obtained from the histogram plots at Fig. 2. However, the H-HSV color plane was excluded from the HOBD calculation. As demonstrated in Fig. 5b, both the WBCs (i.e. ROI_i) and the surrounding RBCs exhibit the same hue, which impairs the initial localization of the ROI_i. Hence, CP_1 used this color plane. Accordingly, the seven extracted features were derived from the intensity values of the G-RGB color plane. To select the most relevant features and improve the classification performance, the extracted features were ranked using the supervised Inf-FS method. Accordingly, the ranked feature vector from the highest to the least significant feature was ordered as follows: α_{max}, Entropy, Energy, M, μ_2, μ_3 and μ_4.

This order establishes the superiority of the proposed α_{max} as a distinctive feature for the classification of the basophil and eosinophil WBC classes based only on the initial estimated ROI_i. The significance of these features in distinguishing the basophils and eosinophils resides in the intrinsic characteristics of these classes. Basophils are identified by their distinctive coarse texture due to the presence of dense dark-violet granules within the cytoplasm, which

TABLE 1. HOBD calculation for the color spaces for the given sample of basophil and eosinophil images.

Image ID	Color Space	First plane HOBD	Second plane HOBD	Third plane HOBD
Baso image #6	RGB	461.73 (R)	4646.40 (G)	368.72 (B)
	HSV	NA+ (H)	880.12 (S)	344.23 (V)
	CIELAB	36.62 (L)	194.18 (A)	502.21 (B)
	YCbCr	1747.60 (Y)	0.0348 (Cb)	1.06 (Cr)
Baso image #7	RGB	766.96 (R)	4710.08 (G)	276.25 (B)
	HSV	NA+ (H)	1220.36 (S)	224.67 (V)
	CIELAB	43.72 (L)	351.25 (A)	262.23 (B)
	YCbCr	2528.35 (Y)	14.48 (Cb)	0 (Cr)
Eosino image #12	RGB	385.33 (R)	518.39 (G)	304.31 (B)
	HSV	NA+ (H)	264.83 (S)	353.81 (V)
	CIELAB	26.01 (L)	107.95 (A)	219.98 (B)
	YCbCr	186.99 (Y)	0.0042 (Cb)	3.29 (Cr)
Eosino image #13	RGB	350.50 (R)	2566.48 (G)	169.95 (B)
	HSV	NA+ (H)	17.61 (S)	341.58 (V)
	CIELAB	97.59 (L)	108.83 (A)	935.13 (B)
	YCbCr	1132.61 (Y)	0.0107 (Cb)	2.77 (Cr)

hide the nucleus. In contrast, eosinophils have more uniform red-orange granules that do not obstruct the nucleus, which leads to a smoother texture.

Accordingly, these brighter eosinophil granules resulted in smaller intensity values as shown in Fig. 6. Therefore, the bin location of the maximum peak at the initial ROI sub-histogram helped discriminate between the two classes. Fig. 6 shows $\alpha_{\max} \approx 0.4$ for the sample eosinophil image compared to $\alpha_{\max} < 0.3$ for the sample basophil image. Moreover, the variation in texture between the two classes was reflected in the entropy, which describes the homogeneity of the given texture. Thus, the entropy was higher in the basophils due to its coarse granules compared to the eosinophils. The average normalized entropy over the basophil dataset was 0.3937 compared to 0.2420 for eosinophils. As for the mean intensity, the basophils showed higher mean values due to the presence of darker intensities in the WBC, which resulted in average normalized value of 0.39 over the basophil dataset compared with 0.34 for eosinophils.

A sample of the normalized extracted features is shown in 2 for both WBC classes. Moreover, to find the optimum number of ranked features, R_k, the effect of different R_k values on the CP_1 classification performance was investigated.

Several SVM kernels were trained using the R_k features, including the first-order, second-order, third-order polynomials, and Gaussian functions, as shown in Fig. 7. The SVMs were all trained using 5-fold cross-validation for better generalization. So, the dataset was divided into 5 equal folds to find the classifier's overall performance as the average of the 5 runs.

Figure 7 shows that the optimal number of the selected features varies with the characteristics of the SVM kernels, which is an expected outcome, especially with filter-based feature selection approaches. Nonetheless, highest classification performance was obtained using the third-order SVM with the top three features, namely the proposed $\alpha_{\max}$, Entropy, and M, reflecting the location of the histograms' maximum peak, the distributions' randomness, and the distributions' mean value, respectively. In contrast, weakest performance was obtained using the coarse Gaussian SVM with the proposed $\alpha_{\max}$ only. Therefore, a third-order SVM was chosen as the initial classifier of the proposed system with $R_k = 3$. Table 3 validates the classifier's selection

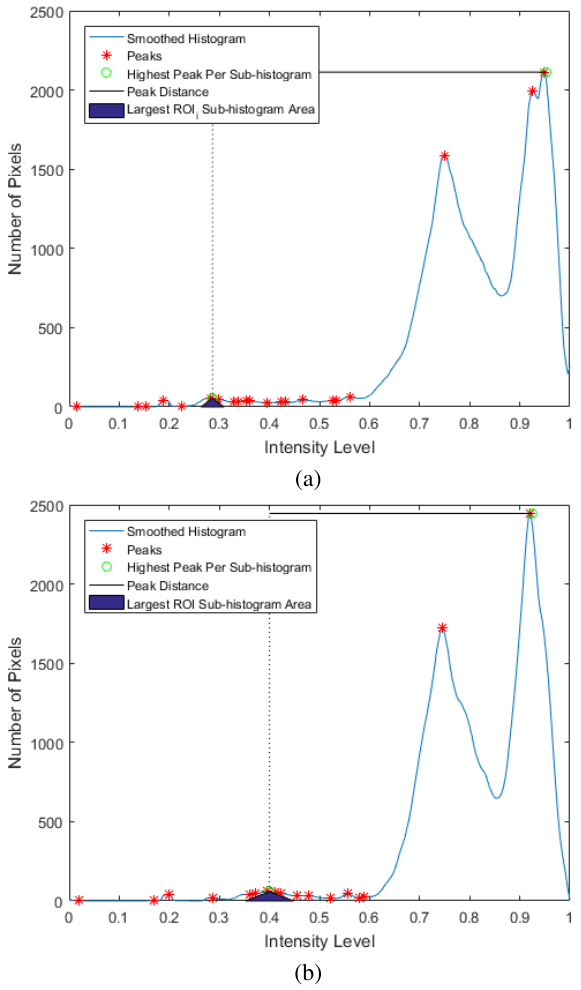

FIGURE 6. Smoothed histogram of green color plane for sample: (a) basophil image (Baso image #13); (b) eosinophil image (Eosi image #13).

TABLE 2. Sample of the normalized extracted features at the initial classification for the given sample of basophil and eosinophil images.

Image ID	M	μ_2	μ_3	μ_4	Energy	Entropy	$\alpha_{\max}$
Baso image #6	0.610	0.472	0.108	0.063	0.597	0.298	0.293
Baso image #7	0.764	0.557	0.052	0.032	0.774	0.522	0.32
Eosino image #12	0.566	0.539	0.142	0.079	0.411	0.199	0.8
Eosino image #13	0.569	0.494	0.118	0.065	0.427	0.237	0.64

TABLE 3. Classification performance metrics of CP_1 using third-order SVM for different numbers of top ranked features.

	Accuracy	Sensitivity	Specificity	F-measure	AUC (ROC)
$R_k = 1$	80.4%	82.1%	79.2%	78.1%	0.86
$R_k = 2$	82.6%	76.9%	86.7%	78.9%	0.85
$R_k = 3$	92.4%	92.3%	92.4%	91.1%	0.95
$R_k = 4$	88.0%	89.7%	86.7%	86.4%	0.88
$R_k = 5$	88.0%	87.1%	88.6%	86.1%	0.90
$R_k = 6$	87.0%	84.6%	88.6%	84.6%	0.90
$R_k = 7$	80.4%	84.6%	90.5%	85.7%	0.91

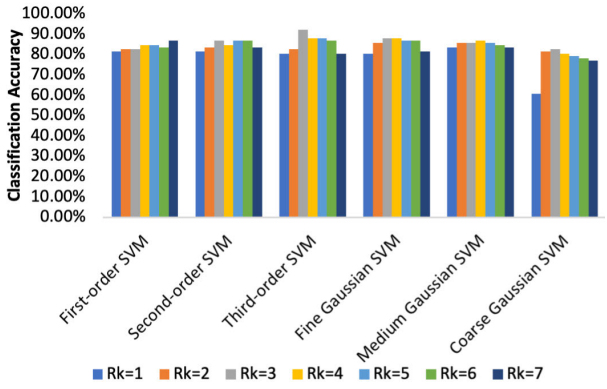

FIGURE 7. Classification accuracy of CP_1 using several SVM kernels for different numbers of top ranked features.

by reporting its classification performance metrics, while demonstrating their values for different R_k values.

The classification performance metrics in Table 3 demonstrate the designated classifier's ability to differentiate between the positive and negative classes, which in our context, are set to be the eosinophil and basophil classes, respectively. Hence, the sensitivity or the 'recall' represents the percentage of the eosinophil images, which are correctly identified, while the specificity holds the same definition but for the basophil images. The F-measure is the weighted harmonic mean of the classifier's precision and recall, where the precision measures the false positives. Generally, these two metrics are commonly in a trade-off. A high F-measure reflects that both precision and recall are equally high values.

B. PHASE 2: FINAL WBC DETECTION BASED ON WAVELET- BASED THRESHOLDING SEGMENTATION

According to the classification predictions, the input pool of WBC images was classified into either basophil or eosinophil, which indicates four probable outcomes for the predicted image. These are:

i) the Baso image is correctly identified (TN);
ii) the Eosino image is correctly identified (TP);
iii) Baso image is falsely classified as Eosino (FP); and
iv) the Eosino image is falsely classified as Baso (FN).

Therefore, the classification decision dictates the application of segmentation Algorithm 1 for the negative predictions (i.e., TN and FN) and Algorithm 2 for the positive predictions (i.e., TP and FP). Figure 8 shows the progression of

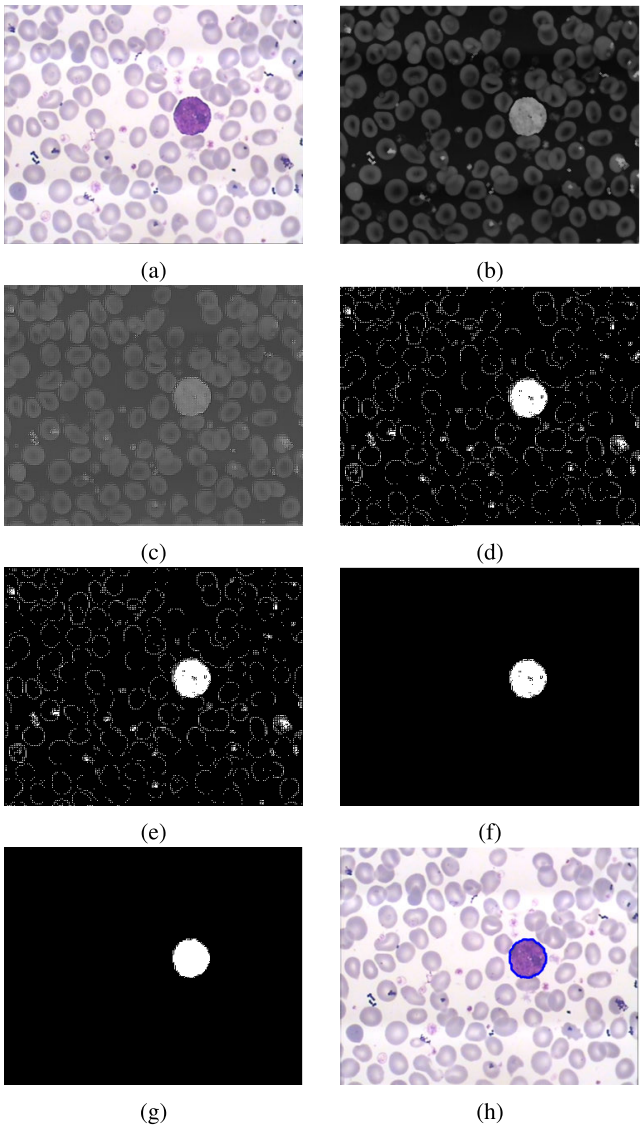

FIGURE 8. Segmented Baso image #41 using algorithm1: (a) input RGB image; (b) C_I complemented L component of CIELAB color space; (c) V inversed DWT image after biorthogonal decomposition; (d) quantized V using the final threshold T_f; (e) after removing border-attached structures; (f) after excluding connected regions with area < 500; (g) after morphological closing and hole filling; (h) the detected boundary of the WBC displayed in blue.

segmentation Algorithm 1 for a TN basophil image (Baso image #41) indicating the processes performed at the pre-processing, the 2-D wavelet decomposition-based thresholding, and the post-processing, while, Fig. 9 shows the progression of segmentation Algorithm 2 for a TP eosinophil image (Eosino image #13).

Table 4 shows sample values of the four thresholds as well as the final threshold. The final threshold was determined by halving the sum of the four thresholds. The maximum threshold was 145.431, which was threshold 1 for Eosino image #10, and its corresponding final threshold was 111.071. Furthermore, for the basophil dataset, a maximum threshold of 66.741 was obtained for threshold 1 in Baso

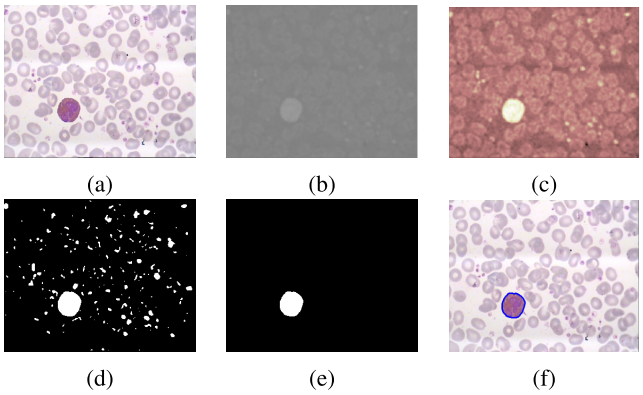

FIGURE 9. Segmented Eosino image #13 using algorithm 2: (a) input RGB image; (b) Cr color plane; (c) cA component of biorthogonal DWT decomposition; (d) quantized cA using the final threshold T_f; (e) after removing border-attached structures and excluding connected regions with area < 500; (f) the detected boundary of the WBC displayed in blue.

image #3, while the maximum final threshold was 90.153 for Baso image #42. Also, for the eosinophil dataset, a maximum threshold of 146.428 was obtained for threshold 1 in Eosino image #14, while the maximum final threshold was 124.269 for Eosino image #3. The values of thresholds 2 to 4 were consistently low (below 60), since the histograms of the wavelet details (i.e. horizontal, vertical, diagonal) were concentrated near the low end of the histogram due to the high presence of low intensity pixels in these images. Thus, the final threshold value will never exceed 255. Hence, the final threshold was used to obtain the segmented image shown in Fig. 8(d) and Fig. 9(d) using the IDWT image and the approximate component for basophils and eosinophils.

Moreover, Fig. 10 shows a sample of the correctly classified images from both classes, where Fig. 10(c) shows the estimated based on the proposed HOBD metric, which indicated the superiority of the G-RGB channel in this process. As previously mentioned, the ROI_i is typically located between $\alpha_1 = 0.2$ and $\alpha_2 = 0.6$. Nevertheless, Fig. 10(d) subjectively evaluates the segmentation process as the segmented ROI_f contour is shown in blue against the ground-truth contour, which is given in red.

For the objective evaluation of the proposed CSRS, the segmentation evaluation metrics are shown in Fig. 11. It demonstrates the effect of the D_v value on the proposed system, as it was varied from 2 to 4, in addition to the segmentation performance in case of applying the same algorithm (1 or 2) for both WBC classes. The illustrated segmentation metrics were computed based on comparing the segmented mask to the ground truth mask. Hence, the definitions of TP, TN refer to the number of correctly identified ROI, or background pixels, respectively. Conversely, the accuracy and specificity does not effectively represent the segmentation performance due to the presence of TN in their equations, which is typically of large value compared to TP, FP, or FN leading to neglecting these terms at the summations. In consequence, the sensitivity, Jaccard index (JAC), and the Dice coefficient are of higher significance. The JAC is the intersection between the ROIs

TABLE 4. Sample and average values of the four wavelet thresholds (thresh.) and the final threshold for the two classes.

	Image ID	Thresh. 1	Thresh. 2	Thresh. 3	Thresh. 4	Final thresh.
Sample threshold values for different Baso images	Baso image #1	63.752	35.863	36.859	27.894	82.184
	Baso image #10	55.784	22.914	24.906	16.937	60.271
	Baso image #11	49.808	18.929	23.909	52.796	72.722
	Baso image #12	53.792	17.933	21.918	49.808	71.725
Average threshold values over the whole Baso dataset		52.702	23.722	27.349	29.229	66.501
Sample threshold values for different Eosino images	Eosino image #1	120.529	12.953	18.930	18.929	85.671
	Eosino image #10	145.431	22.914	32.875	20.922	111.071
	Eosino image #11	108.576	15.941	22.914	24.906	86.169
	Eosino image #12	136.467	21.918	30.882	18.929	104.098
Average threshold values over the whole Eosino dataset		119.648	20.564	23.629	23.374	93.607

of the segmented and ground-truth images divided by their union, while the Dice is twice the overlap area divided by the total number of pixels in both images, so in a perfect scenario these metrics score a 100%.

Figure 11 shows the improved performance of the proposed CSRS with $D_v = 2$ in comparison to $D_v = 3$ or 4, since it demonstrated 86% JAC, 92% Dice, and 96% sensitivity. Moreover, it is evident that applying the same algorithm for both classes reduces the segmentation performance. The proposed reverse classification-segmentation process was performed, where the proposed CSRS was implemented using DWT-based thresholding with $D_v = 2$ in the upcoming evaluations. The detected ROI_f after the final SP_2 segmentation process was applied to a counting process in addition to the CP_2 classification process. The aim of this process was to obtain the number of the detected WBCs in the microscopic images to assist hematological experts in the quantitative analysis of the blood smear images. The counting accuracy of the proposed CSRS method was calculated as the percentage of the class images at which the number of WBCs was accurately detected. Table 5 shows the detected and the true number of WBCs in sample basophil and eosinophil images, in addition to the counting accuracy of both classes.

C. SECOND CLASSIFICATION & COMPUTATIONAL RUNTIME OF PROPOSED SYSTEM

The second classification process was performed to improve the initial classification performance metrics shown at Table 3. This process was performed based on extracting the pre-selected top three features from the segmented ROI. Subsequently, using the third-order SVM, the classification accuracy has increased by nearly 5.2% compared to the initial classification accuracy. The second classification performance metrics are displayed in Table 6.

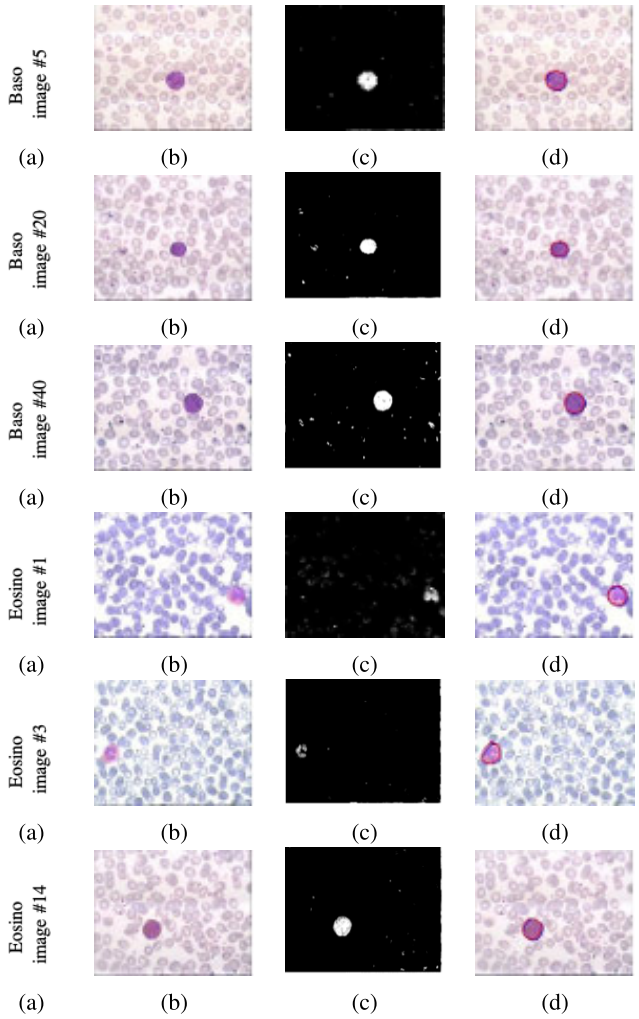

FIGURE 10. Sample WBC segmentation for correctly classified cases, the first three rows are for basophils, and the last three rows are for eosinophils: (a) image ID; (b) original RGB image; (c) ROI_i obtained from initial segmentation process; (d) segmented ROI_f contour represented in blue and ground truth contour represented in red.

TABLE 5. Counting accuracy of detected WBCS using the proposed CSRS.

Class	Image ID	True # of WBCs	Detected # of WBCs
Sample basophil images	Baso image #7	2	2
	Baso image #31	2	2
	Baso image #51	1	1
	Baso image #52	1	1
Basophils counting accuracy		100%	
Sample eosinophil images	Eosino image #13	1	1
	Eosino image #15	1	6
	Eosino image #7	1	1
	Eosino image #8	1	1
Eosinophils counting accuracy		94.8%	

Also, the average runtime of the training and testing phases in seconds were estimated as shown in Table 7, following the sequential processes illustrated at Fig. 3. The training time included the time of the initial ROI feature extraction and selection, where seven features were extracted, and then the top three features were selected, the initial

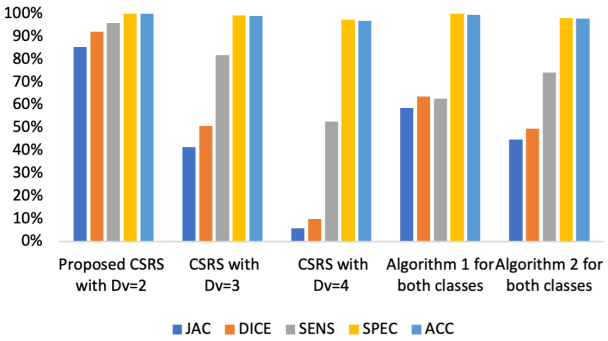

FIGURE 11. Segmentation performance metrics for the proposed CSRS with $D_V = 2, 3$ and 4 compared to applying algorithm 1 or 2 for both WBC classes.

TABLE 6. Third-order SVM second classification CP_2 performance.

Accuracy	Sensitivity	Specificity	F-measure	AUC (ROC)
97.6%	97.1%	98.0%	97.1%	99%

TABLE 7. Average runtime of the training and testing phases of the proposed system.

Process	Training time (s)	Testing time for ten images (s)
Initial ROI feature extraction & selection	1.779	0.011
Initial classification process	12.582	0.055
ROI segmentation process	41.105	5.629
ROI feature extraction process	1.881	0.258
Second classification process	8.102	0.022
Total	65.449	5.975

classifier training time, the ROI segmentation process using the selected algorithm, the extraction of the top three features from the segmented ROI, and the second classifier training time. For the testing time calculation, ten images were applied as the testing input, and the time of each of the pre-mentioned processes were included. However, the initial ROI feature selection process was bypassed at the testing phase. Furthermore, the classifiers testing time was incorporated instead of the training time.

Table 7 establishes that the proposed CSRS is a fast-performing algorithm, where the training process has taken only 65.45 seconds with an average of 5.98 seconds for testing ten input images.

D. COMPARATIVE STUDY OF THE PROPOSED SEGMENTATION WITH OTHER WELL-KNOWN METHODS

The proposed method was also compared with some other segmentation techniques, namely the K-means [44] algorithm and the fuzzy C-means (FCM) [45] algorithm with different number of cluster centers N_c, as shown in Fig. 12 which demonstrates their performance metrics. Figure 12 shows that the proposed CSRS method achieved more precise segmentation results in comparison to both the K-means and the fuzzy C-means at different number of clusters. The displayed

TABLE 8. Average segmentation performance metrics of each class using the proposed CSRS compared to applying each segmentation algorithm on its targeted class.

Class	Method	JAC	Dice	Sensitivity	Specificity	Accuracy
Basophils	Proposed CSRS	0.851	0.919	0.940	0.999	0.999
	Algorithm 1	0.851	0.919	0.937	0.999	0.999
Eosinophils	Proposed CSRS	0.859	0.924	0.989	0.999	0.999
	Algorithm 2	0.796	0.860	0.962	0.998	0.998

segmentation metrics indicated that for the K-means algorithm the JAC, Dice, specificity, and accuracy peaked at $N_c = 3$ compared to $N_c = 2$, and $N_c = 5$. While for the fuzzy C-means, the highest segmentation performance was obtained at $N_c = 10$, where the JAC, Dice, and sensitivity were 12%, 9%, and 26% less than their values using the proposed CSRS method.

It is worth noting that the proposed CSRS method accomplished better segmentation performance in comparison to applying each segmentation algorithm on its targeted class, i.e. Algorithm 1 on basophils, and Algorithm 2 on eosinophils. This is due to the dependency of the proposed method on the image characteristics, which are based on the extracted histogram-based features, rather than the WBC class. Despite the majority of class images following their designated segmentation algorithm, some cases achieved better results using the other segmentation algorithm. For example, Fig. 13 illustrates two basophil images which were misclassified as eosinophil in the initial classification process and subsequently followed segmentation Algorithm 2 instead of segmentation Algorithm 1.

From Fig. 13, it can be concluded that the misclassification has aided the segmentation process, as the initial classification process considers the rough categorization of the input WBC images based on their characteristics, which leads each classified image to follow the suitable segmentation criteria out of the two given algorithms. Nonetheless, the classification performance would also be improved at the subsequent, second classification step CP_2 to accurately determine the WBC classes. Table 8 compares the individual segmentation performance of each class while applying the proposed CSRS against the application of either Algorithm 1 or Algorithm 2 for its given class. Hence, the average segmentation metrics of each class is reported.

IV. PERFORMANCE EVALUATION COMPARISON WITH STATE-OF- THE-ART WORK

Table 9 demonstrates a comparative analysis for highlighting the segmentation performance of the given two WBC classes from the LISC database across some state-of-art studies. Studies that have included the basophils and eosinophils, while evaluating the segmentation performance for each class separately were only considered for comparison. The Similarity Measure was calculated to compare against these studies,

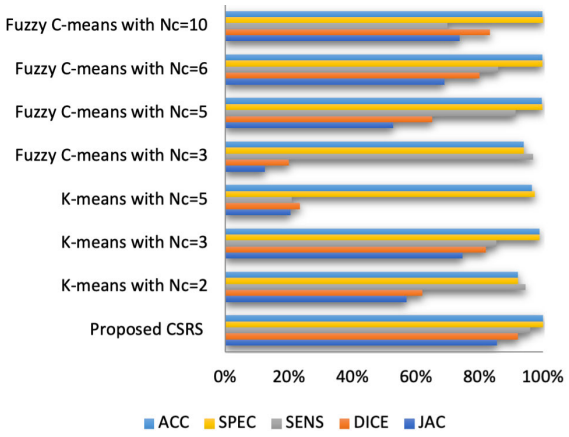

FIGURE 12. Segmentation performance metrics for the proposed CSRS compared to k-means with $N_c = 2, 3, 5$ and FCM with $N_c = 3, 5, 6$ and 10.

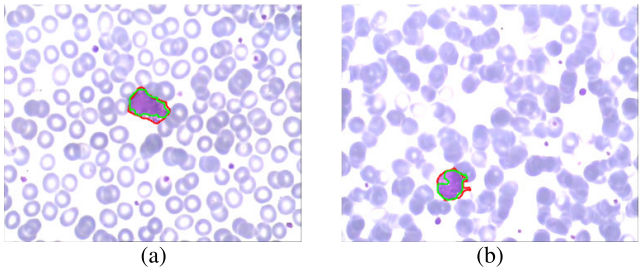

FIGURE 13. Detected boundary of misclassified basophil images: (a) Baso image #48, and (b) Baso image #47 where the red boundary contours the detected area using the proposed CSRS, while the green boundary contours the segmented area using algorithm 1.

which was computed as follows [29]:

$$\text{Similarity Measure} = \frac{A_{\text{seg}} \cap A_{\text{GT}}}{\max(A_{\text{seg}}, A_{\text{GT}})} \times 100 \qquad (19)$$

where A_{seg} is the segmented area using the automated segmentation method, while A_{GT} is the segmented area by the hematological expert. Yet, in studies [32], [46], [47], the segmentation process mainly targeted the WBC nuclei in order to discriminate between the WBC classes. But, in our study we have considered the segmentation of the whole leukocyte cell (i.e. nucleus and cytoplasm) and extracting global features from the segmented cell to determine its class. In [29], [46], [47], both the cytoplasm and nucleus were segmented, and their average Similarity Measure is reported in Table 9.

V. DISCUSSION

In comparison with state-of-art studies using the LISC dataset, our proposed system performs better in terms of segmentation, counting and classification tasks. It is also worth noting that previous studies have adopted deep learning techniques for the detection and classification of WBCs in microscopic images [31], [48]–[51]. However, deep learning techniques usually require large datasets to avoid over-fitting the proposed model. For instance, Kutlu *et al.* [50] combined the LISC dataset and the Blood

TABLE 9. Performance metrics comparative study against the state-of-art studies using the lisc dataset.

Reference	WBC Class	Similarity Measure	JAC	Dice	Sensitivity	Counting Accuracy
Proposed method	**Basophils**	**94.9%**	**0.851**	**0.920**	**0.941**	**100%**
	Eosinophils	**94.1%**	**0.859**	**0.887**	**0.989**	**94.8%**
[29]	Basophils	94.7%	-	-	-	-
	Eosinophils	93.2%	-	-	-	-
[46]	Basophils	90.6%	-	-	-	-
	Eosinophils	84.3%	-	-	-	-
[32]	Basophils	92.5%	-	0.934	-	-
	Eosinophils	82.8%	-	0.864	-	-
[47]	Basophils	91.4%	-	-	-	-
	Eosinophils	86.9%	-	-	-	-

Cell Count and Detection (BCCD) dataset to develop a CNN-based WBC detection and classification model. Accordingly, the ResNet50 architecture achieved 98.48%, and 96.16% accuracies for basophils and eosinophils. Their deep learning methods achieved an average classification accuracy of 97.32% for both classes using a larger dataset, higher computational complexity and processing time. However, our proposed system achieved a 97.6% classification accuracy using the LISC dataset. Additionally, Baydilli *et al.* [51] developed a capsule network for WBC classification, which achieved an average classification accuracy of 96.12% for both classes, which is less than our achieved classification accuracy by nearly 2% using the LISC dataset.

However, it is worth noting that the proposed system failed to handle five images, where some specific cases of microscopic images occurred. These cases included the presence of the WBC at the image corner, as shown in Fig. 14(a) and staining with cytochemical dyes resulting in a comparable chromaticity between the WBC and the surrounding RBCs, as shown in Fig. 14(b).

In addition, we assessed our proposed segmentation system for further verification using the well-known acute lymphoblastic leukemia image database (ALL-IDB) [52]–[54]. The database is composed of two parts: ALL-IDB1, which includes microscopic blood samples from both ALL and non-ALL patients, and ALL-IDB2, which includes the cropped ROI of both normal and lymphoblast cells of ALL-IDB1. However, this database presents a different classification problem, which involves detecting leukemia blast cells. Hence, in the present work, we used the ALL-IDB1 dataset to evaluate our system's segmentation performance in the presence of a large number of WBCs and different illumination conditions, as shown in Fig. 15 compared to the K-means and fuzzy C-means methods applied on ALL-IDB1.

Fig. 15 demonstrates that our proposed method achieved improved segmentation accuracy in comparison to the K-means, while the fuzzy C-means was least accurate. Moreover, Fig. 16 provides further evidence regarding the segmentation accuracy of our proposed method in comparison to the K-means and fuzzy C-means using the ALL-IDB2 dataset.

Fig. 16 shows the improved performance of our method in comparison to the K-means and fuzzy C-means.

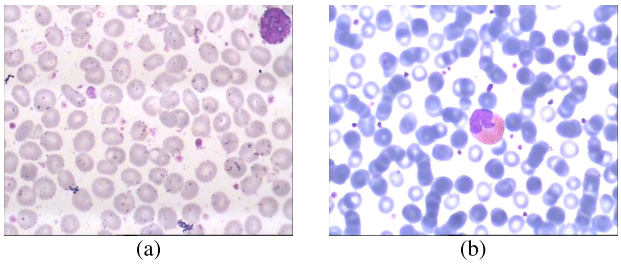

FIGURE 14. Failed segmentation cases due to: (a) the WBC touching the image borders; (b) the WBC chromaticity being comparable to surrounding RBCs.

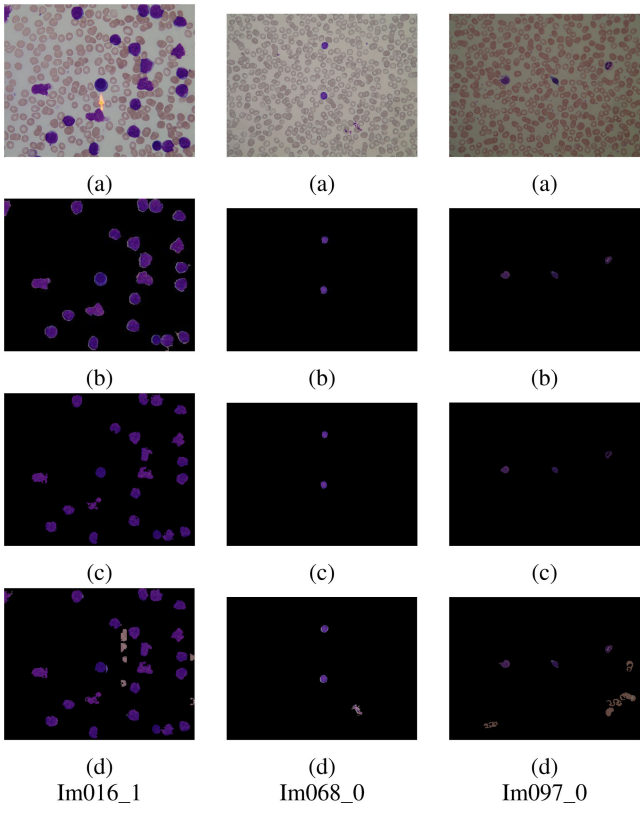

FIGURE 15. Segmentation of sample images from the ALL-IDB1 dataset (given the image ID at the last row): (a) original image; (b) segmentation mask using the proposed method; (c) segmentation mask using K-means; and (d) segmentation mask using fuzzy C-means.

The proposed method achieved an average 96.95% segmentation accuracy, 96.8% sensitivity, 95.5% specificity, 96.% F-measure for both parts of the dataset. In terms of computational complexity, an intel-core i5 computer with 8 GB RAM needed 3.5 seconds to segment the images in the ALL-IDB1 dataset using our proposed algorithms, while 1.2 seconds were required for the images in ALL-IDB2.

On the other hand, our proposed system proved more effective in comparison to other state-of-the-art methods on the ALL-IDB dataset. Scotti [20] proposed an image enhancement-based adaptive method for segmenting white blood cells, which resulted in 92% segmentation accuracy. Moreover, Safuan *et al.* [55] combined color analysis of different color spaces including the RGB, CMYK, and

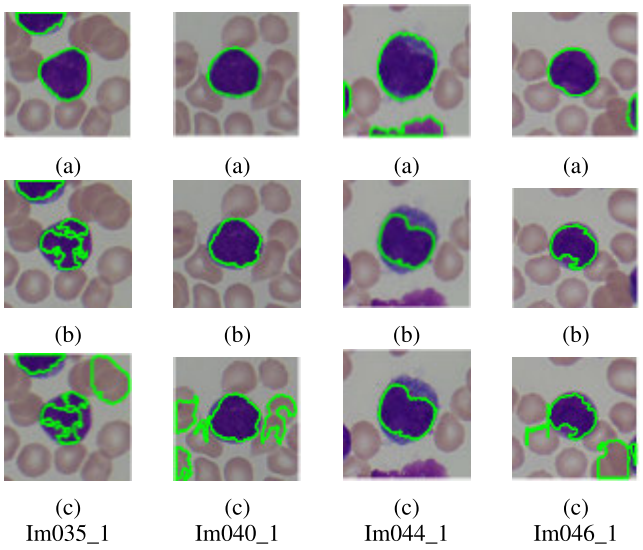

FIGURE 16. Detected WBC contour for sample images from ALL-IDB2 dataset (given the image ID at the last row): (a) using the proposed method; (b) using K-means; and (c) using fuzzy C-means.

HSV with Otsu thresholding followed by morphological filtering and connected component labeling for detecting WBCs. Their results showed that the highest segmentation accuracy was 96.92% using the S component of the HSV color space. Moreover, Li *et al.* [56] proposed a weighted cross-entropy loss function based on class weight and distance transformation weight for deep learning using U-Net for the WBC segmentation using ALL-IDB1, which resulted in 94.92% segmentation accuracy without data augmentation. In addition, our counting accuracy was 93.7% using the entire ALL-IDB dataset, which is 12.7% higher than the accuracy reported by Mahmood *et al.* [57], where color space conversion and Hough transform were used for WBC detection. However, further and future investigations regarding cell overlapping are necessary to improve our counting accuracy. Moreover, a careful investigation into the failed cases is also highly recommended for improving the proposed system performance. Furthermore, an extension to this work may involve developing deep learning-based approaches to mitigate the previously mentioned limitations and drawbacks.

VI. CONCLUSION

Automatic detection, counting and recognition of white blood cells in peripheral blood smear microscopic images can highly contribute to the diagnosis of many blood diseases. However, the morphological variations between the different types of WBCs usually complicate their segmentation process and affect its accuracy. In this study, the basophil and eosinophil were considered as a case study from which these variations were employed to perform an initial classification process prior to deploying the final segmentation algorithm for each class. Accordingly, the proposed HOBD metric determined the green RGB color plane as the most appropriate color plane for performing an initial ROI detection.

After using the green channel histogram-based features that were derived from the initially segmented WBCs, the initial classification process resulted in a 92.4% classification accuracy using the third-order polynomial SVM. Hence, the proposed cascaded classification-segmentation reversible system (CSRS) provided a tailored wavelet transform-based segmentation algorithm for each of these classes. In comparison to current state of the art, which achieved a similarity index of 94.70% for basophils and 93.22% for eosinophils, our segmentation process demonstrated a higher similarity index of 94.9% for basophils and 94.1% for eosinophils for the same dataset. Moreover, an average counting accuracy of 97.4% for both classes was achieved. A second stage classification was carried out after applying the CSRS based on the final segmentation results, which achieved a 5.2% increase in accuracy compared with the initial classification process. Moreover, thanks to the effectiveness and accuracy of the proposed framework, it can be adopted in different image processing applications such as telemedicine, and remote monitoring systems.

REFERENCES

[1] N. M. Karabacak, P. S. Spuhler, F. Fachin, E. J. Lim, V. Pai, E. Ozkumur, J. M. Martel, N. Kojic, K. Smith, P. I. Chen, J. Yang, H. Hwang, B. Morgan, J. Trautwein, T. A. Barber, S. L. Stott, S. Maheswaran, R. Kapur, D. A. Haber, and M. Toner, "Microfluidic, marker-free isolation of circulating tumor cells from blood samples," *Nature Protocols*, vol. 9, no. 3, pp. 694–710, Feb. 2014, doi: 10.1038/nprot.2014.044.

[2] Z. Yang, Z. Zhang, F. Lin, Y. Ren, D. Liu, R. Zhong, and Y. Liang, "Comparisons of neutrophil-, monocyte-, eosinophil-, and basophil-lymphocyte ratios among various systemic autoimmune rheumatic diseases," *Apmis*, vol. 125, no. 10, pp. 863–871, Oct. 2017, doi: 10.1111/apm.12722.

[3] C. D. Stevens and L. E. Miller, *Clinical Immunology and Serology: A Laboratory Perspective*. Philadelphia, PA, USA: FA Davis, 2016.

[4] J. Chung, X. Ou, R. P. Kulkarni, and C. Yang, "Counting white blood cells from a blood smear using Fourier ptychographic microscopy," *PLoS ONE*, vol. 10, no. 7, Jul. 2015, Art. no. e0133489, doi: 10.1371/journal.pone.0133489.

[5] M. I. Razzak and B. Alhaqbani, "Automatic detection of malarial parasite using microscopic blood images," *J. Med. Imag. Health Informat.*, vol. 5, no. 3, pp. 591–598, Jun. 2015, doi: 10.1166/jmihi.2015.1417.

[6] F. Xing and L. Yang, "Robust nucleus/cell detection and segmentation in digital pathology and microscopy images: A comprehensive review," *IEEE Rev. Biomed. Eng.*, vol. 9, pp. 234–263, 2016, doi: 10.1109/RBME.2016.2515127.

[7] T. Bergen, D. Steckhan, T. Wittenberg, and T. Zerfass, "Segmentation of leukocytes and erythrocytes in blood smear images," in *Proc. 30th Annu. Int. Conf. IEEE Eng. Med. Biol. Soc.*, Vancouver, BC, Canada, Aug. 2008, pp. 3075–3078, doi: 10.1109/IEMBS.2008.4649853.

[8] L. Putzu, G. Caocci, and C. Di Ruberto, "Leucocyte classification for leukaemia detection using image processing techniques," *Artif. Intell. Med.*, vol. 62, no. 3, pp. 179–191, Nov. 2014, doi: 10.1016/j.artmed.2014.09.002.

[9] C. Zhang, X. Xiao, X. Li, Y.-J. Chen, W. Zhen, J. Chang, C. Zheng, and Z. Liu, "White blood cell segmentation by color-space-based K-means clustering," *Sensors*, vol. 14, no. 9, pp. 16128–16147, Sep. 2014, doi: 10.3390/s140916128.

[10] J. Zhao, M. Zhang, Z. Zhou, J. Chu, and F. Cao, "Automatic detection and classification of leukocytes using convolutional neural networks," *Med. Biol. Eng. Comput.*, vol. 55, no. 8, pp. 1287–1301, Aug. 2017, doi: 10.1007/s11517-016-1590-x.

[11] H. T. Madhloom, S. A. Kareem, and H. Ariffin, "An image processing application for the localization and segmentation of lymphoblast cell using peripheral blood images," *J. Med. Syst.*, vol. 36, no. 4, pp. 2149–2158, Mar. 2011, doi: 10.1007/s10916-011-9679-0.

[12] Z. Moshavash, H. Danyali, and M. S. Helfroush, "An automatic and robust decision support system for accurate acute leukemia diagnosis from blood microscopic images," *J. Digit. Imag.*, vol. 31, no. 5, pp. 702–717, Apr. 2018, doi: 10.1007/s10278-018-0074-y.

[13] L. Kass, G. J. Harrison, and C. Lindheimer, "A new stain for identification of avian leukocytes," *Biotechnic Histochem.*, vol. 77, no. 4, pp. 201–206, Jul. 2002, doi: 10.1080/bih.77.4.201.206.

[14] C. Di Ruberto, A. Loddo, and L. Putzu, "A leucocytes count system from blood smear images," *Mach. Vis. Appl.*, vol. 27, no. 8, pp. 1151–1160, Oct. 2016, doi: 10.1007/s00138-016-0812-4.

[15] K. Sudha and P. Geetha, "A novel approach for segmentation and counting of overlapped leukocytes in microscopic blood images," *Biocybern. Biomed. Eng.*, vol. 40, no. 2, pp. 639–648, Apr. 2020, doi: 10.1016/j.bbe.2020.02.005.

[16] C. Naugler, E. Mohammed, M. A. Mohamed, and B. Far, "Peripheral blood smear image analysis: A comprehensive review," *J. Pathol. Informat.*, vol. 5, no. 1, p. 9, 2014, doi: 10.4103/2153-3539.129442.

[17] S. Mohapatra, D. Patra, and S. Satpathy, "An ensemble classifier system for early diagnosis of acute lymphoblastic leukemia in blood microscopic images," *Neural Comput. Appl.*, vol. 24, nos. 7–8, pp. 1887–1904, Jun. 2014, doi: 10.1007/s00521-013-1438-3.

[18] J. W. Choi, Y. Ku, B. W. Yoo, J.-A. Kim, D. S. Lee, Y. J. Chai, H.-J. Kong, and H. C. Kim, "White blood cell differential count of maturation stages in bone marrow smear using dual-stage convolutional neural networks," *PLoS ONE*, vol. 12, no. 12, Dec. 2017, Art. no. e0189259, doi: 10.1371/journal.pone.0189259.

[19] B. J. Ferdosi, S. Nowshin, F. A. Sabera, and Habiba, "White blood cell detection and segmentation from fluorescent images with an improved algorithm using K-means clustering and morphological operators," in *Proc. 4th Int. Conf. Electr. Eng. Inf. Commun. Technol. (iCEEiCT)*, Dhaka, Bangladesh, Sep. 2018, pp. 566–570, doi: 10.1109/CEEICT.2018.8628068.

[20] F. Scotti, "Robust segmentation and measurements techniques of white cells in blood microscope images," in *Proc. IEEE Instrum. Meas. Technol. Conf.*, Sorrento, Italy, Dec. 2006, pp. 43–48, doi: 10.1109/IMTC.2006.328170.

[21] X. Li and Y. Cao, "A robust automatic leukocyte recognition method based on island-clustering texture," *J. Innov. Opt. Health Sci.*, vol. 9, no. 1, Jan. 2016, Art. no. 1650009, doi: 10.1142/S1793545816500097.

[22] S. Eom, S. Kim, V. Shin, and B. Ahn, "Leukocyte segmentation in blood smear images using region-based active contours," in *Advanced Concepts for Intelligent Vision Systems*, J. Blanc-Talon, W. Philips, D. Popescu, and P. Scheunders, Eds. Berlin, Germany: Springer, 2006, pp. 867–876.

[23] F. Zamani and R. Safabakhsh, "An unsupervised GVF snake approach for white blood cell segmentation based on nucleus," in *Proc. 8th Int. Conf. Signal Process.*, Guilin, China, vol. 2, 2006, pp. 1–4, doi: 10.1109/ICOSP.2006.345648.

[24] K. Al-Dulaimi, I. Tomeo-Reyes, J. Banks, and V. Chandran, "White blood cell nuclei segmentation using level set methods and geometric active contours," in *Proc. Int. Conf. Digit. Image Comput., Techn. Appl. (DICTA)*, Gold Coast, QLD, Australia, Nov. 2016, pp. 1–7, doi: 10.1109/DICTA.2016.7797097.

[25] A. Sadr, M. Jahed, P. Salehian, and A. Eslami, "Leukocyte's nucleus segmentation using active contour in YCbCr colour space," in *Proc. IEEE EMBS Conf. Biomed. Eng. Sci. (IECBES)*, Kuala Lumpur, Malaysia, Nov. 2010, pp. 257–260, doi: 10.1109/IECBES.2010.5742239.

[26] L. H. Nee, M. Y. Mashor, and R. Hassan, "White blood cell segmentation for acute leukemia bone marrow images," *J. Med. Imag. Health Informat.*, vol. 2, no. 3, pp. 278–284, Sep. 2012, doi: 10.1109/ICoBE.2012.6179038.

[27] M. N. Prasad, K. Prasad, and K. T. Navya, "Color transfer method for efficient enhancement of color images and its application to peripheral blood smear analysis," in *Recent Trends in Image Processing and Pattern Recognition*, K. C. Santosh and R. S. Hegadi, Eds. Singapore: Springer, 2019, pp. 134–142, doi: 10.1007/978-981-13-9184-2_12.

[28] L. A. Bhavnani, U. K. Jaliya, and M. J. Joshi, "Segmentation and counting of WBCs and RBCs from microscopic blood sample images," *Int. J. Image, Graph. Signal Process.*, vol. 8, no. 11, pp. 32–40, Nov. 2016, doi: 10.5815/ijigsp.2016.11.05.

[29] S. H. Rezatofighi and H. Soltanian-Zadeh, "Automatic recognition of five types of white blood cells in peripheral blood," *Comput. Med. Imag. Graph.*, vol. 35, no. 4, pp. 333–343, Jun. 2011, doi: 10.1016/j.compmedimag.2011.01.003.

[30] N. Theera-Umpon, "White blood cell segmentation and classification in microscopic bone marrow images," in *Fuzzy Systems and Knowledge Discovery*, L. Wang and Y. Jin, Eds. Berlin, Germany: Springer, 2005, pp. 787–796, doi: 10.1007/11540007_98.

[31] S. Nazlibilek, D. Karacor, T. Ercan, M. H. Sazli, O. Kalender, and Y. Ege, "Automatic segmentation, counting, size determination and classification of white blood cells," *Measurement*, vol. 55, pp. 58–65, Sep. 2014, doi: 10.1016/j.measurement.2014.04.008.

[32] S. Sapna and A. Renuka, "Computer-aided system for leukocyte nucleus segmentation and leukocyte classification based on nucleus characteristics," *Int. J. Comput. Appl.*, vol. 42, no. 6, pp. 622–633, Aug. 2020, doi: 10.1080/1206212X.2020.1726013.

[33] A. Materka and M. Strzelecki, "Texture analysis methods—A review," Tech. Univ. Lodz, Inst. Electron., Brussels, Belgium, Tech. Rep. COST B11, 1998, p. 4968, vol. 10, no. 1.97.

[34] D. M. U. Sabino, L. F. Costa, E. G. Rizzatti, and M. A. Zago, "Toward leukocyte recognition using morphometry, texture and color," in *Proc. 2nd IEEE Int. Symp. Biomed. Imag., Macro Nano*, Arlington, VA, USA, Apr. 2004, pp. 121–124, doi: 10.1109/ISBI.2004.1398489.

[35] G. Chandrashekar and F. Sahin, "A survey on feature selection methods," *Comput. Elect. Eng.*, vol. 40, no. 1, pp. 16–28, Jan. 2014, doi: 10.1016/j.compeleceng.2013.11.024.

[36] G. Roffo, S. Melzi, U. Castellani, A. Vinciarelli, and M. Cristani, "Infinite feature selection: A graph-based feature filtering approach," *IEEE Trans. Pattern Anal. Mach. Intell.*, early access, Jun. 16, 2020, doi: 10.1109/TPAMI.2020.3002843.

[37] A. Zien, G. Rätsch, S. Mika, B. Schölkopf, T. Lengauer, and K.-R. Müller, "Engineering support vector machine kernels that recognize translation initiation sites," *Bioinformatics*, vol. 16, no. 9, pp. 799–807, Sep. 2000, doi: 10.1093/bioinformatics/16.9.799.

[38] J.-W. Seo and S. D. Kim, "Novel PCA-based color-to-gray image conversion," in *Proc. IEEE Int. Conf. Image Process.*, Melbourne, VIC, Australia, Sep. 2013, pp. 2279–2283, doi: 10.1109/ICIP.2013.6738470.

[39] J. A. Bhutto, T. Lianfang, Q. Du, T. A. Soomro, Y. Lubin, and M. F. Tahir, "An enhanced image fusion algorithm by combined histogram equalization and fast gray level grouping using multi-scale decomposition and gray-PCA," *IEEE Access*, vol. 8, pp. 157005–157021, 2020, doi: 10.1109/ACCESS.2020.3018264.

[40] W. A. Mustafa, H. Yazid, and S. B. Yaacob, "Illumination normalization of non-uniform images based on double mean filtering," in *Proc. IEEE Int. Conf. Control Syst., Comput. Eng. (ICCSCE)*, Penang, Malaysia, Nov. 2014, pp. 366–371, doi: 10.1109/ICCSCE.2014.7072746.

[41] P. Peng, P. Alencar, and D. Cowan, "A software framework for PCa-based face recognition," in *Proc. IEEE Int. Conf. Softw. Sci., Technol. Eng. (SWSTE)*, Beer Sheva, Israel, Jun. 2016, pp. 7–16, doi: 10.1109/SWSTE.2016.11.

[42] N. Otsu, "A threshold selection method from gray-level histograms," *IEEE Trans. Syst., Man, Cybern.*, vol. SMC-9, no. 1, pp. 62–66, Jan. 1979, doi: 10.1109/TSMC.1979.4310076.

[43] M. Filho, Z. Ma, and J. M. R. S. Tavares, "A review of the quantification and classification of pigmented skin lesions: From dedicated to hand-held devices," *J. Med. Syst.*, vol. 39, no. 11, p. 177, Nov. 2015, doi: 10.1007/s10916-015-0354-8.

[44] S. Ray and R. H. Turi, "Determination of number of clusters in K-means clustering and application in colour segmentation," in *Proc. 4th Int. Conf. Adv. Pattern Recognit. Digit. Techn.*, Calcutta, India, 1999, pp. 137–143.

[45] P. Viswanathan, "Fuzzy C means detection of leukemia based on morphological contour segmentation," *Procedia Comput. Sci.*, vol. 58, pp. 84–90, Jan. 2015, doi: 10.1016/j.procs.2015.08.017.

[46] A. Tareef, Y. Song, W. Cai, Y. Wang, D. D. Feng, and M. Chen, "Automatic nuclei and cytoplasm segmentation of leukocytes with color and texture-based image enhancement," in *Proc. IEEE 13th Int. Symp. Biomed. Imag. (ISBI)*, Prague, Czech Republic, Apr. 2016, pp. 935–938, doi: 10.1109/ISBI.2016.7493418.

[47] A. Tareef, Y. Song, D. Feng, M. Chen, and W. Cai, "Automated multi-stage segmentation of white blood cells via optimizing color processing," in *Proc. IEEE 14th Int. Symp. Biomed. Imag. (ISBI)*, Melbourne, VIC, Australia, Apr. 2017, pp. 565–568, doi: 10.1109/ISBI.2017.7950584.

[48] H. Fan, F. Zhang, L. Xi, Z. Li, G. Liu, and Y. Xu, "LeukocyteMask: An automated localization and segmentation method for leukocyte in blood smear images using deep neural networks," *J. Biophotonics*, vol. 12, no. 7, Jul. 2019, Art. no. e201800488, doi: 10.1002/jbio.201800488.

[49] I. Naz, N. Muhammad, M. Yasmin, M. Sharif, J. H. Shah, and S. L. Fernandes, "Robust discrimination of leukocytes protuberant types for early diagnosis of leukemia," *J. Mech. Med. Biol.*, vol. 19, no. 6, Sep. 2019, Art. no. 1950055, doi: 10.1142/S0219519419500556.
[50] H. Kutlu, E. Avci, and F. Özyurt, "White blood cells detection and classification based on regional convolutional neural networks," *Med. Hypotheses*, vol. 135, Feb. 2020, Art. no. 109472, doi: 10.1016/j.mehy.2019.109472.
[51] Y. Y. Baydilli and Ü. Atila, "Classification of white blood cells using capsule networks," *Comput. Med. Imag. Graph.*, vol. 80, Mar. 2020, Art. no. 101699, doi: 10.1016/j.compmedimag.2020.101699.
[52] V. Piuri and F. Scotti, "Morphological classification of blood leucocytes by microscope images," in *Proc. IEEE Int. Conf. Comput. Intell. Meas. Syst. Appl. (CIMSA)*, Boston, MA, USA, Jul. 2004, pp. 103–108, doi: 10.1109/CIMSA.2004.1397242.
[53] F. Scotti, "Automatic morphological analysis for acute leukemia identification in peripheral blood microscope images," in *Proc. IEEE Int. Conf. Comput. Intell. Meas. Syst. Appl. (CIMSA)*, Taormina, Italy, Jul. 2005, pp. 96–101, doi: 10.1109/CIMSA.2005.1522835.
[54] R. D. Labati, V. Piuri, and F. Scotti, "All-IDB: The acute lymphoblastic leukemia image database for image processing," in *Proc. 18th IEEE Int. Conf. Image Process.*, Brussels, Belgium, Sep. 2011, pp. 2045–2048, doi: 10.1109/ICIP.2011.6115881.
[55] S. N. M. Safuan, M. R. M. Tomari, and W. N. W. Zakaria, "White blood cell (WBC) counting analysis in blood smear images using various color segmentation methods," *Measurement*, vol. 116, pp. 543–555, Feb. 2018, doi: 10.1016/j.measurement.2017.11.002.
[56] H. Li, X. Zhao, A. Su, H. Zhang, J. Liu, and G. Gu, "Color space transformation and multi-class weighted loss for adhesive white blood cell segmentation," *IEEE Access*, vol. 8, pp. 24808–24818, 2020, doi: 10.1109/ACCESS.2020.2970485.
[57] N. H. Mahmood, P. C. Lim, S. M. Mazalan, and M. A. A. Razak, "Blood cells extraction using color based segmentation technique," *Int. J. Life Sci. Biotechnol. Pharma Res.*, vol. 2, no. 2, pp. 2250–3137, 2013.

AMIRA S. ASHOUR received the M.Sc. degree in electrical engineering (image processing based nondestructive evaluation performance), and the Ph.D. degree in smart antenna from the Department of Electronics and Electrical Communication Engineering, Faculty of Engineering, Tanta University, Egypt. She has been an Assistant Professor and the Head of Department with the Department of Electronics and Electrical Communication Engineering, Faculty of Engineering, Tanta University, since 2016. She is also the ICT Manager of Huawei Academy and a Research and Development Member with the Faculty of Engineering, Tanta University. She published 91 journal articles and conference proceedings and edited/authored about 20 books (Elsevier/Springer). Her research interests include biomedical engineering, medical devices, medical image and signal processing, medical imaging, ablation therapy, machine learning, optimization, smart antenna, target tracking, and direction of arrival estimation. She is an editorial board member of several reputable journals.

MARAM A. WAHBA received the B.Sc. and M.Sc. degrees in electrical engineering from the Faculty of Engineering, Tanta University, Egypt, in 2013. She is currently an Assistant Lecturer with the Department of Electronics and Electrical Communications, Faculty of Engineering, Tanta University. Her research interests include machine learning, pattern recognition, image processing, and medical imaging.

RAMI GHANNAM (Senior Member, IEEE) received the B.Eng. degree in electronic engineering from King's College London, the DIC and M.Sc. degrees from Imperial College London, and the Ph.D. degree from the University of Cambridge, in 2007. He is currently a Lecturer (an Assistant Professor) of electronic and nanoscale engineering with the University of Glasgow. He held previous industrial positions at Nortel Networks and IBM Research GmbH. His research interests include photonics, sensors, and engineering education. He is a Senior Fellow of Glasgow's RET Scheme. He was awarded the Siemens Prize. He serves as the Scotland Regional Chair for the IEEE Education Society.